

Two-dimensional modeling of diamond growth by microwave plasma activated chemical vapor deposition: Effects of pressure, absorbed power and the beneficial role of nitrogen on diamond growth

Michael N.R. Ashfold^{a,*}, Yuri A. Mankelevich^b

^a School of Chemistry, University of Bristol, Bristol BS8 1TS, UK

^b Skobeltsyn Institute of Nuclear Physics, Moscow State University, Leninskie gory, Moscow 119991, Russia

ARTICLE INFO

Keywords:

Diamond
Microwave
Plasma
Chemical vapor deposition
Modeling
Growth rate
Nitrogen

ABSTRACT

A two-dimensional (2D(r , z)) self-consistent model developed and validated in previous studies of diamond deposition processes in microwave (MW) plasma activated chemical vapor deposition reactors is applied in a systematic study of ways in which the gas pressure (over the range $p = 75$ –350 Torr) and absorbed power ($P = 1$ –3 kW) affect the plasma parameters, species distributions and diamond deposition processes from a gas mixture (1%CH₄/H₂ with 60 ppm added N₂) at substrate temperatures ($T_s = 1073$ and 1323 K) and diameters ($d_s = 32$ –100 mm). A more limited set of process conditions for a 0.006%N₂/4%CH₄/H₂ gas mixture and $T_s = 1038$ –1153 K are investigated also. The study traces variations in the global distributions of electron concentration, electron and gas temperature, absorbed power density, key species concentrations and the hydrocarbon interconversion reactions, with particular focus on the radial profiles of CH₃ radical and H atom concentrations just above the substrate and on predicted diamond growth rates, $G(r)$. The results and the trends revealed when varying p and P should help guide future optimizations of deposition regimes. The absorbed power density is shown to exhibit quite steep gradients in both the radial (r) and axial (z) directions. This, and the finding of significant power absorption beyond the glowing plasma region, limits the utility of the oft-quoted ‘averaged power density’ as a parameter. The modeling also highlights the essential 2D character of the hydrocarbon interconversion and diffusion transfer processes, which challenges the applicability of any 1D modeling of such MW plasmas. Trace additions of N₂ to a MW plasma activated CH₄/H₂ gas mixture have negligible effect on the plasma parameters or chemistry yet are known to boost the diamond growth rate. A semi-empirical expression for $G(r)$ is developed further to explicitly include the effects of added N₂ and a new mechanistic picture presented to account for the observed N-induced enhancements in G . This picture invokes stable moieties such as that formed by CH₂ insertion into a C-N dimer bond on the 2×1 reconstructed (100) diamond surface as ‘anchor’ sites that enable shorter CH₂ surface migration lengths and more step-edges for irreversible incorporation of such migrating groups on the growing diamond surface.

1. Introduction

The recent explosive increase in both the number and the range of theoretical studies employing numerical modeling, quantum mechanical calculations and purpose-developed codes is enabling stunning advances in many areas of the chemical, physical, biological and other sciences, leading to breakthroughs and new technologies, materials and products and revisions and refinements of much prior understanding. However, the capabilities of numerical modeling in some specific areas, for example in describing the complex and inter-related processes in

plasma processing and the plasma-activated chemical vapor deposition (PACVD) of thin films, are arguably less evident and indeed disputed by some parts of the experimental community. Such skepticism may be well-founded in the case of an unverified or incomplete model that has been imposed on raw data. In contrast, thorough and consistent numerical models, verified on a large and diverse body of experimental data, can be very useful: indeed, sometimes they may be the only possible tool for explaining and understanding the observed phenomena, key processes and effects.

The role and importance of such two-dimensional (2D) modeling are

* Corresponding author.

E-mail addresses: mike.ashfold@bristol.ac.uk (M.N.R. Ashfold), ymankelevich@mics.msu.ru (Y.A. Mankelevich).

<https://doi.org/10.1016/j.diamond.2023.110097>

Received 15 February 2023; Received in revised form 17 May 2023; Accepted 6 June 2023

Available online 7 June 2023

0925-9635/© 2023 The Authors. Published by Elsevier B.V. This is an open access article under the CC BY license (<http://creativecommons.org/licenses/by/4.0/>).

clearly evident in a long-running series of combined theoretical-experimental studies of diamond CVD processes activated by microwave (MW) plasmas in a range of gas mixtures [1–3]. The 2D modeling provides the distributions of numerous gas phase species and allows determination of the optimal process parameters (e.g. gas pressure, absorbed power, C_2H_2/H_2 input gas mixture, etc.) to address the needs of the grower (e.g. deposition rate and uniformity, film quality, etc.) and a rationale for the main trends. In the case of diamond growth by MW PACVD, however, the long (~three decade) search for optimal reactor configurations and diamond deposition regimes is still ongoing. Systematic variations of process parameters like the absorbed power P , gas pressure p , source gas flow rate and mixing ratio (e.g. CH_4/H_2 , with or without deliberate (or otherwise) trace additives such as N_2 and/or O_2), substrate temperature T_s , etc., and the modes and geometry of the MW PACVD reactor (e.g. reactor size, geometry and position of the substrate holder, cooling schemes, etc.) provide a massive amount of experimental data for analyzing parametric dependences of diamond growth rates and film quality and uniformity. Some of these dependences are not universal, i.e. can be reactor-specific. For example, the growth rate in some PACVD reactors reportedly increases sharply with p [4] whereas in others it stays near constant [5]. Identifying effects attributable to just one parameter is complicated in many studies where more than one parameter are varied simultaneously as, for example, in studies where p and P are both progressively increased [6].

Quantitative detection of species important for diamond growth (e.g. CH_3 radicals and H atoms) just above the substrate is experimentally challenging. Modeling remains the best tool for probing these and many other important species, and their process-dependent spatial distributions in MW PACVD reactors. 1D(z) [7,8], 1D(r) [7] and 2D(r, z) [3,9–18] models (where r and z are, respectively, radial and axial coordinates defined relative to an origin at the center of the substrate surface) have all been applied to aspects of the diamond deposition process, plasma parameters and, in some cases, species distributions in different PACVD reactors and gas mixtures. The focus of this article is complementary 2D(r, z) modeling and experimental studies of different input gas mixtures and spatially-dependent and process-dependent species concentrations in the Bristol MW PACVD reactor. Early studies revealed (i) that the methyl radical concentration, $[CH_3](r, z)$, exhibited an annular (shell-like) structure with comparable radial and axial concentration gradients and (ii) a complex picture of hydrocarbon interconversions throughout the whole reactor with three main zones [1,19,20]. Both these findings serve to illustrate the limitations of applying 1D modeling when the species concentrations and plasma parameters are clearly of higher dimensionality and flag the need for caution when considering results and predictions derived from such 1D modeling. Some of these challenges are discussed briefly in Section 2.5 of this article.

The deposition processes in the more complex gas mixtures used for X-doped ($X = B, N, Si$, etc.) diamond growth and some of the puzzling trends observed experimentally are inexplicable without companion modeling. For example, the first comprehensive study of MW activated $B_2H_6/CH_4/Ar/H_2$ plasmas operating under conditions relevant to B-doped diamond (BDD) growth observed an order of magnitude ‘spike’ in the B atom and BH radical concentrations when adding methane with flow rates in the range $0 \leq F(CH_4) \leq 5$ standard cm^3 per minute (sccm) to a pre-existing $B_2H_6/Ar/H_2$ plasma, rather than the expected progressive decrease of $[BH_x]$ ($x = 0, 1$) with increasing $F(CH_4)$ due to the conversion $BH_x \rightarrow H_yCBH_z$. 2D model calculations succeeded in explaining this unexpected ‘explosion’ of $[BH_x]$ concentrations by recognizing the presence of trace (~10 ppm) O_2 within the process gas mixture and developing a H/B/C/O reaction mechanism that included the following key conversions: $BH_x \leftrightarrow H_yBC_z$ (involving C_2H_2 and C_2H_4) and $BH_x \rightarrow H_yBO \rightarrow H_zCOBH_y \rightarrow BH_x$ (via reaction with, or activation by, H_2O , CH_x species and/or H atoms) [21]. Such a sharp dependence of [B] (identified as the main doping species in BDD growth) upon starting $F(CH_4)$ hinted at the possibility of growing ultrathin (nanometric or

‘delta’) layers of BDD with differing (by an order of magnitude or more) doping levels by limited changes in $F(CH_4)$ in an optimally chosen B/C/H/O gas mixture. Addition of 0.2% O_2 to a plasma activated 0.2% $CH_4/0.001\%B(CH_3)_3/H_2$ gas mixture was later shown to reduce the local B-doping level in a single crystal BDD sample by up to two orders of magnitude [22]. Controlled addition of H_2S to a MW plasma activated $B_2H_6/CH_4/H_2$ gas mixture has also been shown to reduce the $[BH_x]$ concentration available for BDD growth, allowing opportunities to form delta layers of more heavily B-doped diamond [23]. No high-level modeling of the B/C/H/S reactive system has yet been reported, but similarities between the B/C/H/S and B/C/H/O chemical mechanisms can be expected, e.g. BH_x loss via reaction with H_2S (cf. H_2O) and the formation of boron scavengers like H_xBS , cf. H_xBO [21,24].

Si-doped diamond is currently attracting much interest because of the attractive optical properties of the negatively charged silicon-vacancy (SiV^-) defect [25]. A recent experimental/modeling study of MW plasma activated Si/C/H plasmas [10] determined that Si atoms and/or SiC_2 species are likely to be the most abundant gas-phase Si-containing species just above the growing diamond surface and thus the most likely carriers of the silicon incorporated in CVD diamond. Other important features arising from that study included recognition that (i) the total silicon content within the reactor volume is sensitive to silicon deposition (at the reactor walls) and release via etching (by H atoms) of such deposits, of the substrate itself (if silicon) and of any fused silica components within the MW reactor, (ii) electron impact excitation and chemiluminescent reactions both contribute to the observed $^1Si^*$, $^3Si^*$, and SiH^* emissions, and (iii) the high concentrations of ground state Si atoms throughout the reactor volume can attenuate the $^3Si^*$ emission. Nonetheless, the study also showed that optical emission spectroscopy (OES) measurements of $^1Si^*$ or $^3Si^*$ atoms should both provide a reliable measure of the Si content in the core of a MW activated Si/C/H plasma [10] – a key requirement for growers who aspire to apply OE methods for process control.

The benefits of trace amounts of nitrogen in enhancing the growth rates of both polycrystalline [26,27] and homoepitaxial [28–33] diamond have long been recognized and the nitrogen-vacancy (NV) defects in diamond (and the optical accessibility of single spin quantum states) continue to attract huge interest in quantum technologies and in applications for electric and magnetic field measurements [34]. 2D modeling of MW activated N/H [35] and N/C/H [2,3] gas mixtures has revealed that most (>99.5%) of the input N_2 eludes chemical processing and is exhausted unaltered from the reactor. A small fraction of the input N_2 is decomposed, however, by electron impact excitation or by reaction, primarily with CH_x ($x = 0, 1$) species or, when electronically excited, with H atoms. The near surface N atom concentration is calculated to be at least ten times larger than that of other potentially reactive N-containing species like NH, NH_2 or CN. The near-substrate gas phase $[N]/[CH_3]$ concentration ratios are so low (e.g. $\sim 2 \times 10^{-5}$ for a 4% CH_4/H_2 plasma with 60 ppm added N_2 operating in the Bristol reactor at $p = 150$ Torr, with an absorbed power $P = 1.4$ kW and total flow rate $F_{total} \sim 600$ sccm) that it remains challenging to conceive of mechanisms wherein the incorporation of such small concentrations of any N-containing precursor can result in up to an order of magnitude increases in growth rate [36]. We recently suggested [3] that an N-containing species on the diamond surface can act as an ‘anchor’ site which facilitates the growth of small islands that serve as additional step-edges for further irreversible accommodation of surface migrating CH_2 groups and develop this idea further in Section 4 below.

The 2D(r, z) modeling reported here focuses on common trends and on how variations in p and P affect the diamond deposition processes. The 2D(r, z) self-consistent model has been developed, refined and verified in many prior combined theoretical/experimental studies of the Bristol MW PACVD reactor [2,3,10–21,24,35,37–42]. Section 2 provides a summary of the model and reports calculated spatial distributions of key plasma parameters and important species, including CH_3 radicals and H atoms close above the substrate surface, as functions of p and P

(for more than one substrate diameter (d_s) and temperature (T_s)). Some of the recognized shortcomings of 1D modeling are also emphasized and illustrated at this point. The parameterized expression for the diamond growth rate, G , is reprised in Section 3, where the effects on G of adding N_2 to MW activated CH_4/H_2 mixtures and of changing the substrate diameter and temperature are all considered further. Section 4 offers a new mechanistic perspective on this growth enhancement, that invokes N-based ‘anchor’ sites and their beneficial effects with regard to limiting the migration and encouraging the incorporation of CH_2 groups on the growing diamond surface [3].

2. MW plasma parameters and species spatial distributions at different gas pressures and absorbed powers; 2D vs 1D modeling

All results reported in this study of various regimes for diamond CVD processes driven by MW activated dilute N/C/H plasmas were obtained using the 2D(r, z) self-consistent model that has been tested, enhanced and verified against absorption and OES data for many different MW activated gas mixtures including H_2 [41], Ar/ H_2 and Kr/ H_2 [42], CH_4/H_2 [11–19,39,40], SiH_4/H_2 and $SiH_4/CH_4/H_2$ [10] and $N_2/CH_4/H_2$ [2,35] plasmas operating in the Bristol reactor. The radius and height (the distance between the top surface of the reactor base plate and the lower surface of the quartz window that defines the top of the cylindrical reactor) are $R_r = 6.1$ and $H_r = 6.1$ cm, respectively, and the substrate (a 3 mm-thick, 32 mm-diameter disc unless specified otherwise) is seated centrally on a thin spacer wire on the base plate. The gas mixture (0.006% $N_2/1\%CH_4/H_2$) was fixed for all regimes studied in this section, as was the substrate temperature, $T_s = 1073$ K (again except when specified otherwise), while p and P were varied over wide ranges.

The specific blocks of the model address the plasma-chemical and electron (e) kinetics, heat, mass and species transfer and gas-surface interactions, and solve Maxwell's equations to calculate the spatially dependent MW electromagnetic (EM) fields and MW power. The electron energy distribution functions (EEDFs) for all cells in the (r, z) grid are calculated from the Boltzmann equation and sets of e-H, e- H_2 , e- C_yH_x , e- $C_yH_xN_z$ and e-ion collision cross sections (for different local mixture compositions, reduced electric fields and gas temperatures, T_g) to provide the necessary rate coefficients for the blocks describing the plasma-chemical kinetics and the EM fields. The full reaction mechanism involves 53 species, including key neutral species ($H(n=1-3)$, H_2 , C, CH , 3CH_2 , 1CH_2 , CH_3 , CH_4 , C_2H_x ($x=0-6$), C_yH_x ($y=3,4, x=0-2$), NH_x ($x=0-3$), H_xCN ($x=0-2$), N_2 , selected excited electronic states of N_2 and H_2 , $N(^2D)$ and $C(^1D)$ atoms, $CH(A^2\Delta)$, $C_2(d^3\Pi_g)$ and $C_2(a^3\Pi_u)$ radicals, electrons and the following ions: H^+ , H_2^+ , H_3^+ , $C_2H_2^+$, $C_2H_3^+$, $C_4H_3^+$, NH_4^+ , N_2H^+ and $HCNH^+$). The N/C/H plasma chemistry is described using a total of 535 reactions [3]. The modeling necessarily includes plasma-chemical processes like electron impact ionization (EI), excitation (EIE) and dissociation (EID), excitation of rovibrational states of H_2 and their vibrational-translational (V-T) and rotational-translational (R-T) relaxations, associative ionization, ion conversion and electron-ion recombination reactions, and a few important reactions involving electronically excited species. Key reaction mechanisms, plasma parameters and deposition processes were reprised recently [3] and in two previous papers [2,35].

2.1. MW plasma parameters and species distributions returned by the 2D (r, z) self-consistent model

Here we illustrate how variations in p and P affect the 2D distributions of selected key species concentrations and plasma parameters. Figs. 1 and 2 show, respectively, the response of the calculated 2D(r, z) distributions of the electron concentration, n_e , and electron temperature, T_e , with increasing p (at fixed $P = 1.4$ kW) and increasing P (at fixed $p = 150$ Torr). Unsurprisingly, the absorbed power density, PD, increases with p (the maximal power density, PD_{max} , is found to vary as $\sim p^{1.75}$ over the investigated range) mainly because of the increased rates

of rovibrational excitation of H_2 and C_2H_2 and of elastic collisions of electrons. As a result, the volume of the hot plasma core (V_p , the central region with the highest values of n_e and T_e) shrinks with increasing p (Figs. 1 and 2(a)). The maximal gas temperatures ($T_{gmax} = 2910, 2985, 3196$ and 3430 K for $p = 60, 75, 150$ and 350 Torr, respectively) and electron concentrations n_{emax} also increase with p ($n_{emax} \sim p^{1.1}$), but the maximal electron temperatures, T_{emax} , in the plasma core decrease. The decline in T_{emax} reflects the substantial increase in all ionization sources (i.e. associative ionization via the $H(n \geq 2) + H_2 \rightarrow H_3^+ + e$ and $H(n \geq 3) + H(n=1) \rightarrow H_2^+ + e$ reactions and the ionization of H, H_2 and C_yH_x species by electron impact) as a result of the increased concentrations of all these neutral species at higher p . As a result, the n_e value required to absorb a given power at higher pressures (notwithstanding the smaller volume of the plasma core) is reached at lower values of T_e .

The axial distribution $T_e(r=0, z)$ at low pressures (e.g. at $p = 75$ Torr, Fig. 1(b)) shows a second local maximum, $T_{emax2} \sim 0.8$ eV, near the quartz window. This second maximum increases in relative importance upon reducing p further and is predicted to reach a similar T_e value to the near-substrate T_{emax} value at $p = 60$ Torr. This offers further illustration of the value of the 2D modeling. 60 Torr is outside the range of stable operation of the Bristol reactor ($p \geq 75$ Torr for $P = 1.4$ kW), but the 2D modeling reveals formation of this secondary plasma region near the quartz window with similar T_{emax2} and n_{emax2} values to those (T_{emax} and n_{emax}) in the main plasma core above the substrate (Fig. 1(a)). This secondary plasma region at $p = 60$ Torr induces excessive heating of the quartz window; the predicted temperature at the center of the plasma side of the quartz window $T_q(r=0)$ is ~ 1020 K, cf. $T_q(r=0) \sim 615, \sim 555$ and ~ 590 K for $p = 75, 150$ and 350 Torr, respectively (with $P = 1.4$ kW in all cases). Such overheating, along with incident H atoms and ions (especially hot $C_yH_x^+$ ions) can be expected to cause some etching of the quartz window and the creation of volatile products (e.g. $H_xSiO_z, SiH_x, SiC_yH_x$, etc.). Such species can react further with hydrogen and with hydrocarbons [10] and result in eventual re-deposition of Si-based material on the reactor walls and windows. The presence of such SiO_z, C_yH_x species in the reactor volume and, possibly, the simultaneous deposition/etching of these species on the mirrors could explain the time-evolving broadband visible absorption identified in previous cavity ring down spectroscopy studies of MW plasma activated C/H/Ar gas mixtures operating at $p < 150$ Torr [37,43].

In contrast to the effects of varying pressure, increasing P results in an expansion of the hot plasma core and modest declines in n_{emax} and T_{emax} (Fig. 2) and in the maximal gas temperature, $T_{gmax} \approx 3200, 3196$ and 3140 K for $P = 1, 1.4$ and 3 kW, respectively (all at $p = 150$ Torr). We note that the maximum value at high P (e.g. 3 kW) is realized in the off-axial region (i.e. is shifted to the region above the substrate edge, as shown in Fig. 2(b)). This can be traced to the electric field enhancement at the substrate edge. Fig. 3 shows the calculated radial profiles of the reduced electric field, $|E|/(N \times a)$ (where N is the concentration of neutral particles, a is the pressure dependent factor $a = (1 + \omega^2/\nu^2)^{0.5}$, and ω and ν are respectively the MW frequency $\omega = 2\pi \times 2.45$ GHz and the electron collision frequency) [3,40], at various heights z for $P =$ (a) 1.4 kW ($r < 0$ in Fig. 3) and (b) 3 kW ($r > 0$), all at $p = 150$ Torr. At low P , the plasma core is compact and the $\{|E|/(N \times a)\}(r)$ profiles decline steeply between the central region ($r = 0$) and the substrate edge ($r = -16$ mm). The electric field enhancement at the substrate edge is obvious at small z , but the value of $|E|/(N \times a)$ is lower than at $r = 0$ (Fig. 3(a)) and thus does not critically affect the spatial structure of the plasma.

In contrast, the expansion of the plasma (and the electric field) at high P reduces the radial decline of $|E|/(N \times a)$ and is predicted to lead to another, larger, maximum in $|E|/(N \times a)$ above the substrate edge (Fig. 3(b)), which manifests in off-axis maxima in n_{emax}, T_{emax} (Fig. 2(b)) and T_{gmax} at high absorbed powers. For $P = 3$ kW, the difference between $T_{gmax} = 3140$ K and the maximal axial temperature at $r = 0$ (3108 K) with the standard substrate ($d_s = 32$ mm) is small (limited to $\sim 1\%$). Additional calculations were run to explore how the reduced electric

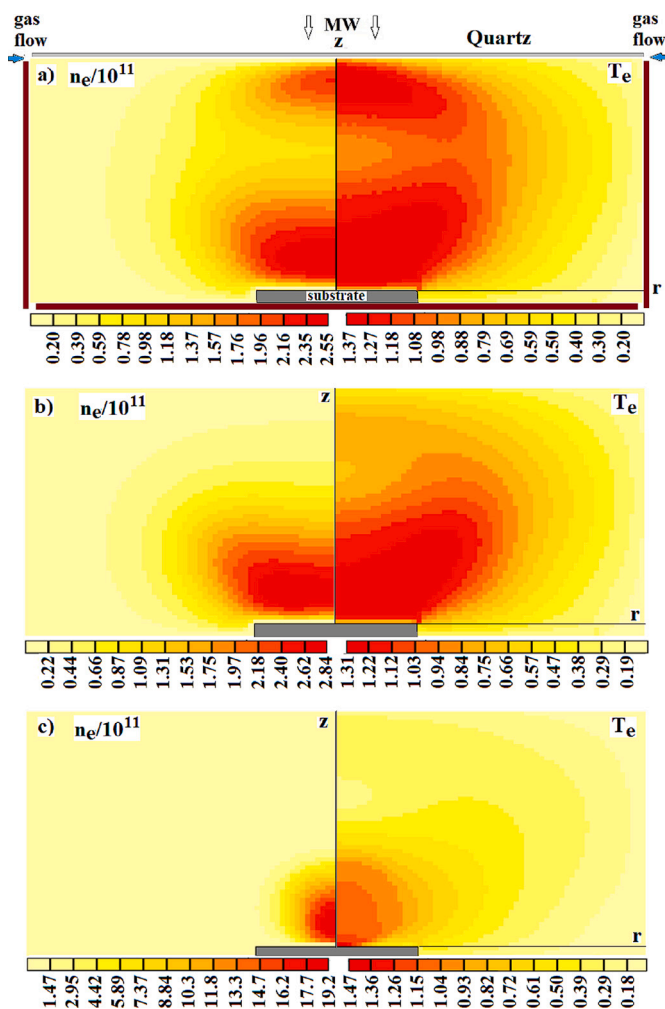


Fig. 1. Calculated 2D(r, z) distributions of the electron concentration, n_e (in cm^{-3} , left), and electron temperature, T_e (in eV, right) for MW activated 0.006%N₂/1% CH₄/H₂ gas mixtures at an absorbed power $P = 1.4$ kW and pressures $p =$ (a) 60 Torr, (b) 75 Torr and (c) 350 Torr. The substrate diameter, $d_s = 32$ mm, and temperature, $T_s = 1073$ K, and the colour scale used in each panel spans 13 equal intervals. Key elements of the reactor (substrate, quartz window, the incident MW radiation, and the (radially symmetric) gas input) are illustrated in panel (a), which also defines the r and z axes used in the modeling with origin ($r = 0, z = 0$) at the top center of the substrate.

field was affected by changing the substrate diameter. As Fig. 2(c) shows, increasing d_s to 100 mm (maintaining $P = 3$ kW and $p = 150$ Torr) largely preserves the 2-D spatial distributions of n_e and T_e , reduces both $n_{e,\text{max}}$ and $T_{e,\text{max}}$ and eliminates any edge enhancement effect on the plasma core region. However, the differences between the overall and the on-axis maxima of these distributions are predicted to be much reduced, down to $\sim 2\%$ for $d_s = 100$ mm (cf. differences of $\sim 11\%$ (for n_e) and $\sim 6.5\%$ (for T_e) when $d_s = 32$ mm).

Fig. 4 shows z -profiles of the power density, PD, and the H($n = 3$) concentration (i.e. the population in the upper state associated with the experimentally measured H Balmer- α (H_{α}) emission) at various r values for $p =$ (a) 75 and (b) 150 Torr and $P = 1.4$ kW. Clearly, the regions of MW power absorption and plasma emissions expand with decreasing pressure. Experimentalists often use the volume of glowing plasma as a proxy for the volume used in estimating the PD but, as Fig. 4 shows, such a procedure is likely to overestimate the real PD. The 2D modeling shows that a substantial fraction (up to 30–50 %) of the MW power is absorbed in the cooler plasma outside the volume exhibiting H_{α} (and other H*), C₂* and CH* emissions [11,12,38].

The 2D modeling also provides insights into how the absorbed MW power is partitioned and transformed. The major fraction (typically $>90\%$) of the power absorbed by the electrons is partitioned into vibrational (i.e., E \rightarrow V) and rotational (i.e., E \rightarrow R) excitation of (mainly) H₂ and C₂H₂ (the dominant hydrocarbon in the hot plasma region) and is lost through elastic collisions of electrons with H₂, H, C₂H₂, etc. The remainder is expended on EID of H₂, C₂H₂, etc., and electronic excitation of H₂, H and C _{γ} H _{γ} species. Fast V \rightarrow T and R \rightarrow T energy transfer from the rovibrationally excited species through collision with H atoms results in translational excitation of the latter, which then dissipates as gas heating. The absorbed power transferred from the electrons to the gas dissipates further by (i) thermal conduction to the substrate and reactor walls and (ii) chemical conversions and radiation losses. For the present MW plasma operating at $p = 150$ Torr and $P = 1.4$ kW, the relative importance of the conduction loss pathways (1.29 kW in total) is illustrated by the following partitioning: $\sim 22\%$ to the substrate, $\sim 42\%$ to the base plate, $\sim 15\%$ to the top window and $\sim 21\%$ to the sidewalls of the cylindrical reactor. (The corresponding values for the plasma at $p = 75$ Torr, $P = 1.4$ kW are $\sim 14\%$, $\sim 38\%$, $\sim 20.5\%$, $\sim 27.5\%$, amounting

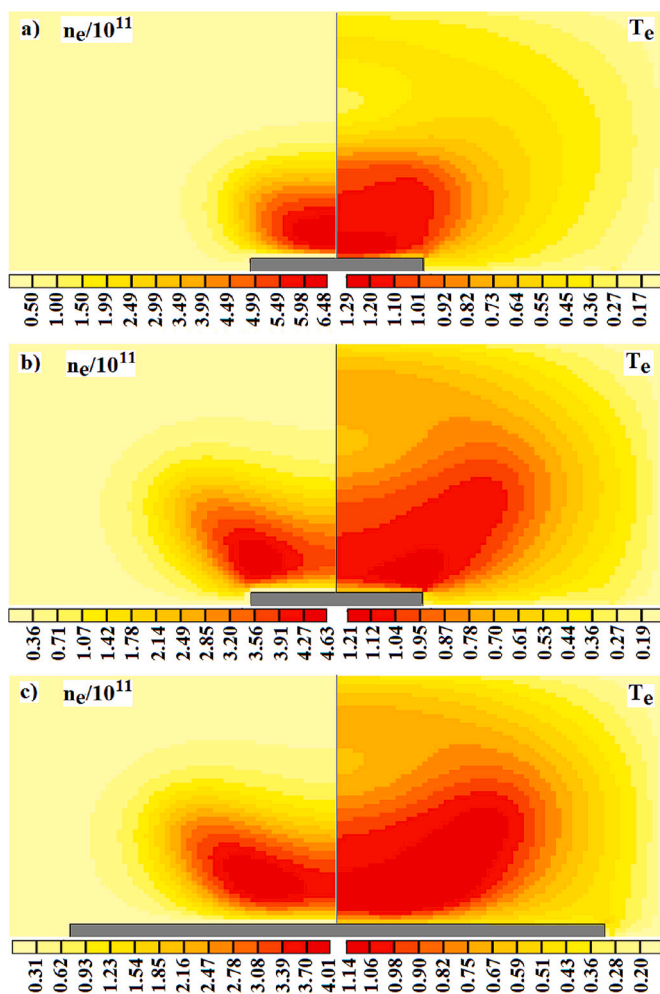


Fig. 2. Calculated 2D(r, z) distributions of the electron concentration, n_e (in cm^{-3} , left), and electron temperature, T_e (in eV, right) for MW activated 0.006% N_2 /1% CH_4/H_2 gas mixtures at $p = 150$ Torr and absorbed powers $P =$ (a) 1.4 kW and (b) 3 kW (both for $d_s = 32$ mm) and (c) 3 kW, for $d_s = 100$ mm. All other details are as in Fig. 1.

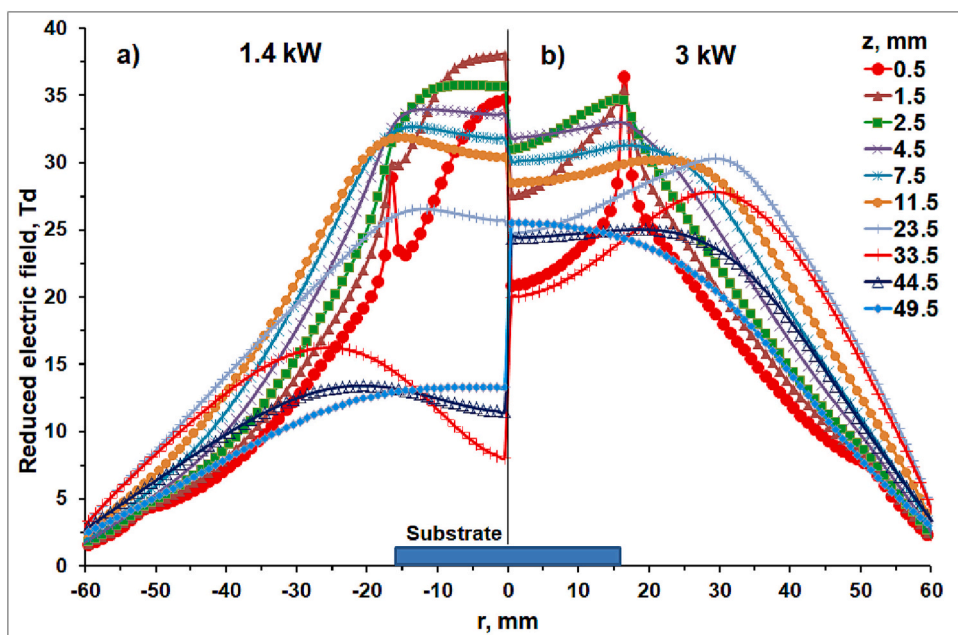


Fig. 3. Calculated r -profiles of the reduced electric fields $|E|/(N \times a)$ in Td for MW activated 0.006% N_2 /1% CH_4/H_2 gas mixtures at $P =$ (a) 1.4 kW ($r < 0$) and (b) 3 kW ($r > 0$), at $p = 150$ Torr and at various heights z above the substrate surface.

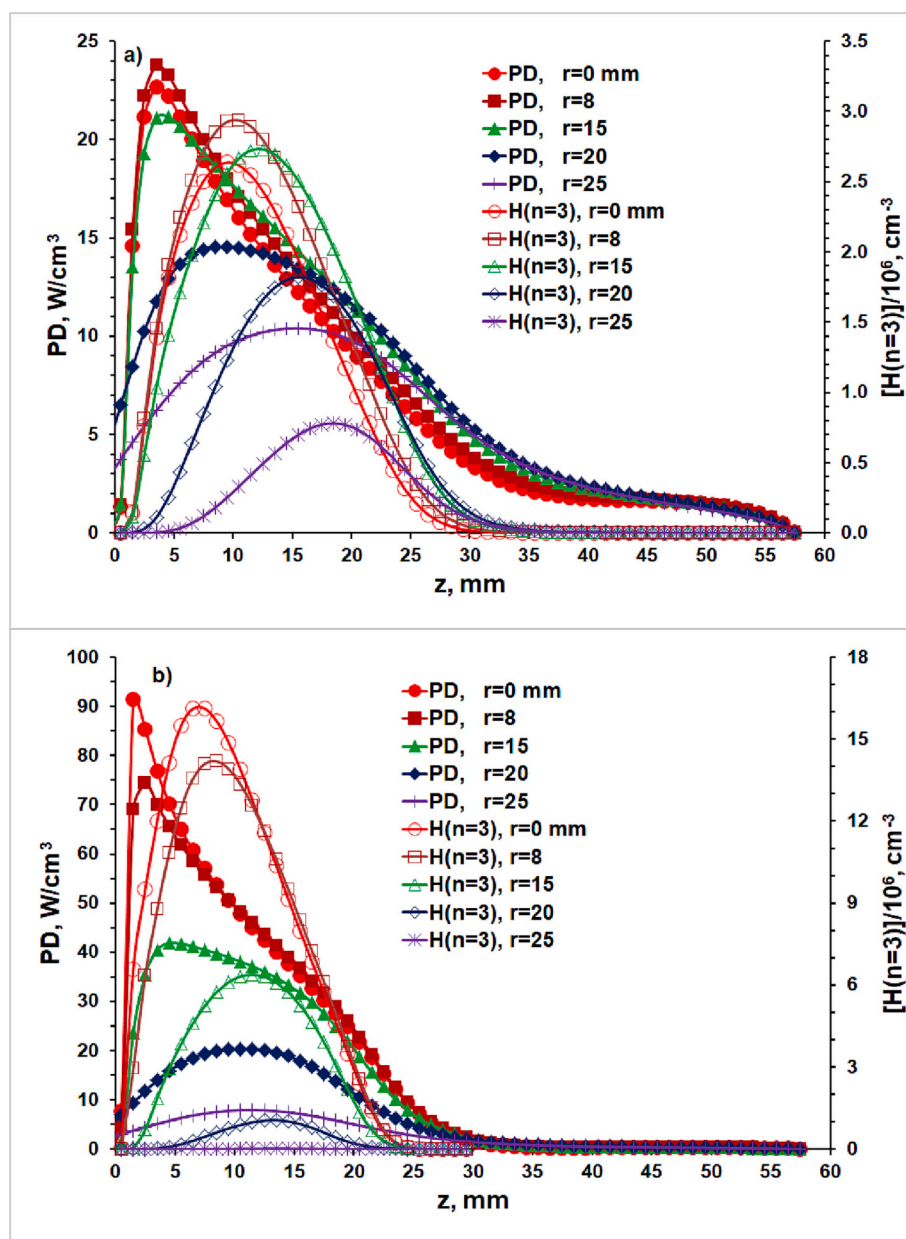


Fig. 4. Calculated z -profiles of the power density (PD) and the $H(n=3)$ concentration for MW activated 0.006% N_2 /1% CH_4 / H_2 gas mixtures at $p =$ (a) 75 and (b) 150 Torr, at $P = 1.4$ kW and at various radial coordinates r as shown in the inset box.

to 1.37 kW in total, consistent with the larger, more diffuse plasma region evident from comparing Figs. 2(a) and 1(b)). The minor fraction of the total absorbed power dissipated via chemical conversions and radiation losses (pathway (ii) above) is mostly consumed in thermal dissociation of H_2 and subsequent loss of H atoms in gas phase reactions and by addition/recombination reactions at the substrate. For example, the present 2D modeling suggests that H atom addition/recombination reactions at $p = 150$ and 75 Torr (and $P = 1.4$ kW) contribute, respectively, 95 W and 28 W to substrate heating. The foregoing responses of the plasma parameters to variations in p and P are reflected in the spatial distributions of the gas temperature, T_g , and the various species concentrations. To set the scene, Fig. 5 shows 2D(r, z) plots of (a) CH_3 concentration, $[CH_3]$, (b) CH_4 and (d) C_2H_2 mole fractions ($X(CH_4)$ and $X(C_2H_2)$), respectively) and (c) T_g , for $p = 150$ Torr and $P = 1.4$ kW. Annular (or 'shell'-shaped) $[CH_3](r, z)$ distributions are consistently found – both in previous [1,19] and the present modeling – for a wide

range of process conditions and gas mixtures. The CH_3 concentrations maximize just outside the hot plasma core region, as had been recognized in earlier 1D(r) and 1D(z) modeling studies [7]. In this region, the CH_3 formation rate via the key reversible reaction (1) is maximal [1,19]. Recognition of this source hints at the possibility of increasing $[CH_3]$ adjacent to the substrate surface by injecting CH_4 into the boundary layer [6] or by raising the plasma region a little and thereby propagating the optimal shell region over the entire substrate. The latter possibility has been realized by designing a reactor wherein the substrate could be translated by up to a few mm relative to the EM focus, thereby offering some control of the discharge shape, size and position and enabling growth rate enhancements of up to a factor of two [5]. In the cooler near substrate regions, the recombination reaction (2) also provides a significant contribution to CH_3 loss (with a rate comparable to that of reaction (–1)) and, at sufficiently low substrate temperatures (e.g. $T_s < 1200$ K), reaction (3) constitutes another significant CH_3 production

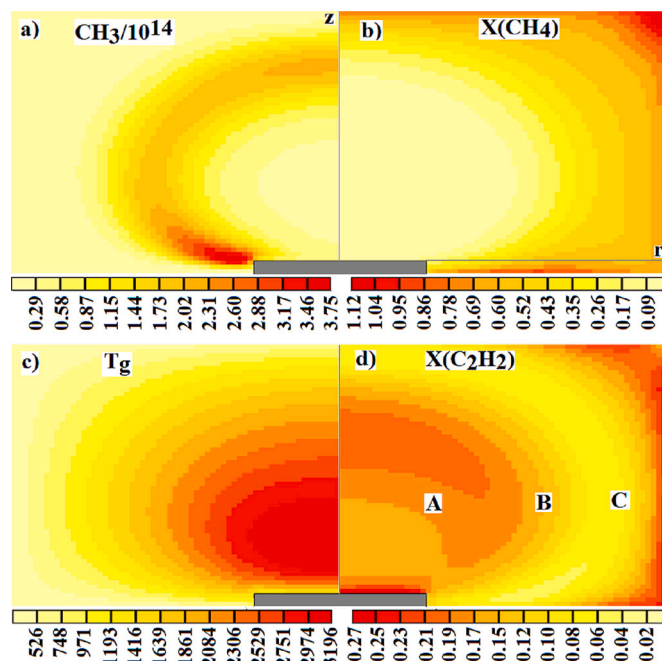


Fig. 5. Calculated 2D(r, z) distributions of (a) CH₃ concentration (in cm⁻³), (b) CH₄ mole fraction (in %) (c), gas temperature, T_g (in K) and (d) C₂H₂ mole fraction (in %) for a MW activated 0.006%N₂/1%CH₄/H₂ gas mixture at $p = 150$ Torr, $P = 1.4$ kW and $T_s = 1073$ K. The three main zones of hydrocarbon conversion are indicated as A, B, and C (see text) and all other details are as for Fig. 1.

route.



The near balance between the backward and forward reactions in equilibrium (Eq. (1)) determines the methyl radical concentrations throughout the whole reactor volume apart for the near-substrate region and close to the reactor walls, where reactions (2) and (3) provide local perturbations, and implies relation (4):

$$[\text{CH}_3] = [\text{H}] \times (k_1 \times [\text{CH}_4] + 2 \times k_3 \times [\text{C}_2\text{H}_5]) / ([\text{H}_2] \times (k_{-1} + k_2 \times [\text{H}])) \quad (4)$$

$[\text{CH}_3]$ depends on the spatial distributions of T_g directly (via the temperature dependent rate coefficients $k_i(T_g)$ presented in Table 1) and indirectly (via the thermodynamically-induced increase [13] in hydrocarbon mole fraction upon approaching the substrate) and on the concentrations $[\text{H}]$ and $[\text{CH}_4]$ (and $[\text{C}_2\text{H}_5]$), which show opposite

behaviors. CH₄ is introduced as part of the input gas flow and shows maximal concentrations near the reactor walls and minimal concentrations in the hot plasma core (Fig. 5). In contrast, the concentration of H atoms (mainly formed by thermal dissociation of H₂) maximizes in the hot plasma core and decays diffusively to the substrate and to all reactor walls, as shown below (Figs. 6 and 7). Three regions supporting different dominant C_yH_x interconversion behaviors are illustrated in Fig. 5: the central, hot plasma region A, and two hemispherical shells, B and C, characterized by different average T_g and $[\text{H}]$ values [1]. Region B supports CH₄ decomposition and conversion to (mainly) C₂H₂, at gas temperatures $1400 \text{ K} < T_g < 2200 \text{ K}$. (This multi-step conversion involves the net consumption of four H atoms per $2\text{CH}_4 \rightarrow \text{C}_2\text{H}_2$ conversion [19]). The reverse $\text{C}_2\text{H}_2 \rightarrow 2\text{CH}_4$ conversion is dominant in region C, where $T_g < 1400 \text{ K}$. This latter conversion is activated by H atoms but leads to no net H atom consumption [19]. The near-substrate region shows a compressed replica of the behaviors in region B and, to a lesser extent, C for the respective ranges of T_g , $[\text{C}_y\text{H}_x]$, $[\text{H}]$ and $[\text{H}_2]$, but with much steeper axial gradients of T_g and most species concentrations. Reaction (3) is an important contributor to the conversion between the

Table 1

Most important reactions (and rate coefficients, k_i) for the production and loss of CH₃ radicals just above the substrate center for MW activated 0.006%N₂/ $x\%$ CH₄/H₂ gas mixtures. The last three columns show illustrative reaction rates, R_i , for the following conditions: I; $x = 1$, $p = 150$ Torr, $P = 1.4$ kW, $d_s = 32$ mm, $T_s = 1073$ K (for which the temperature jump $\Delta T = 88$ K, (i.e. $T_g = T_s + 88$ K)), II; $x = 1$, $p = 150$ Torr, $P = 1.4$ kW, $T_s = 1323$ K ($\Delta T = 90$ K), III; $x = 4$, $p = 250$ Torr, $P = 3.5$ kW, $T_s = 1123$ K ($\Delta T = 72$ K). The quoted $k_i(T_g)$ expressions (approximated from the GRI-Mech mechanism [50] for the limited temperature range $T_g = 900$ – 2000 K) are in units of cm³ s⁻¹ and cm⁶ s⁻¹ (for the two- and three-body reactions, respectively), the reaction rates R_i (at the stated T_g values) are in cm⁻³ s⁻¹ and the temperatures are in K. The last row of the table illustrates the thermodynamically driven depletion of the carbon balance $X(\text{C})$ in the near-substrate region at each temperature.

i	Reaction	Rate coefficient, k_i	R_i (I)	R_i (II)	R_i (III)
1	CH ₄ + H → CH ₃ + H ₂	$1.1 \times 10^{-15} T_g^{1.62} \exp(-5455/T_g)$	1.21×10^{18}	8.46×10^{17}	8.79×10^{18}
-1	CH ₃ + H ₂ → CH ₄ + H	$4.9 \times 10^{-18} T_g^{1.9} \exp(-4900/T_g)$	1.48×10^{18}	1.49×10^{18}	9.25×10^{18}
2	CH ₃ + H + H ₂ → CH ₄ + H ₂	$1.31 \times 10^{-22} T_g^{2.5} \exp(1400/T_g)$	1.31×10^{18}	1.51×10^{17}	1.24×10^{19}
3	C ₂ H ₅ + H → CH ₃ + CH ₃	$1.47 \times 10^{-6} T_g^{-1} \exp(-600/T_g)$	2.02×10^{17}	1.14×10^{16}	5.24×10^{18}
	T_s , K		1073	1323	1123
	%CH ₄ ; p , Torr		1%; 150	1%; 150	4%; 250
	Carbon balance, $X(\text{C})$, %		0.69	0.59	2.84

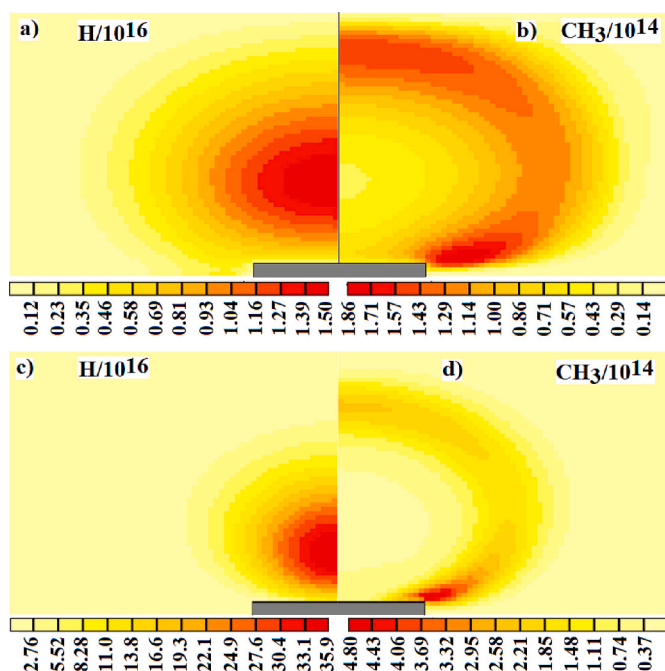
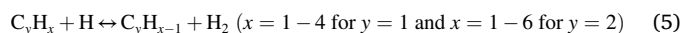


Fig. 6. Calculated 2D(r, z) distributions of (a) and (c) H atom concentrations and (b) and (d) CH_3 radical concentrations for MW activated 0.006% N_2 /1% CH_4/H_2 gas mixtures at $P = 1.4$ kW and $p = 75$ Torr (panels (a) and (b)) and 350 Torr (panels (c) and (d)). All other details are as for Fig. 1.

C_2H_x and CH_x families in the near-substrate region.

The central hot region, **A**, is characterized by near equilibrium distributions in both the CH_x ($x = 0-4$) and C_2H_x ($x = 0-6$) groups. The fast forward and reverse H-shifting reactions (5) are almost in balance within each group. The identification of regions **A-C**, each with their own characteristic chemistries, provides obvious rationales for (i) the local maximum of $[\text{CH}_3]$ in shell **B** and (ii) the observed insensitivity of the deposition process to the specific choice of hydrocarbon process gas C_yH_x . But the demonstrably 2D character of the hydrocarbon interconversions and diffusional transfer will necessarily provide substantial challenges to any attempt at reliable 1D modeling of such MW plasma-activated processes.



2.2. Effects of varying gas pressure on the CH_3 radical and H atom distributions

2D modeling allows calculation of the global distributions of all species, including the CH_3 radicals and H atoms that are key to determining diamond growth rates, $G(r)$, as functions of gas pressure. Fig. 6 shows calculated 2D(r, z) distributions for these two species at $p = 75$ and 350 Torr with $P = 1.4$ kW. (The corresponding plot for $[\text{CH}_3]$ at $p = 150$ Torr was shown in Fig. 5(a)). The spatial extent of the H atom distribution visibly shrinks with increasing p , as does the annular zone **B** associated with maximal CH_3 concentrations. The maximal H atom concentration, $[\text{H}_{\text{max}}]$, increases near quadratically with p (i.e. $[\text{H}_{\text{max}}] \sim p^2$; $[\text{H}_{\text{max}}] = 1.5 \times 10^{16}$, 7.7×10^{16} and 3.6×10^{17} for $p = 75$, 150 and 350 Torr, respectively), while the maximal CH_3 concentration shows a

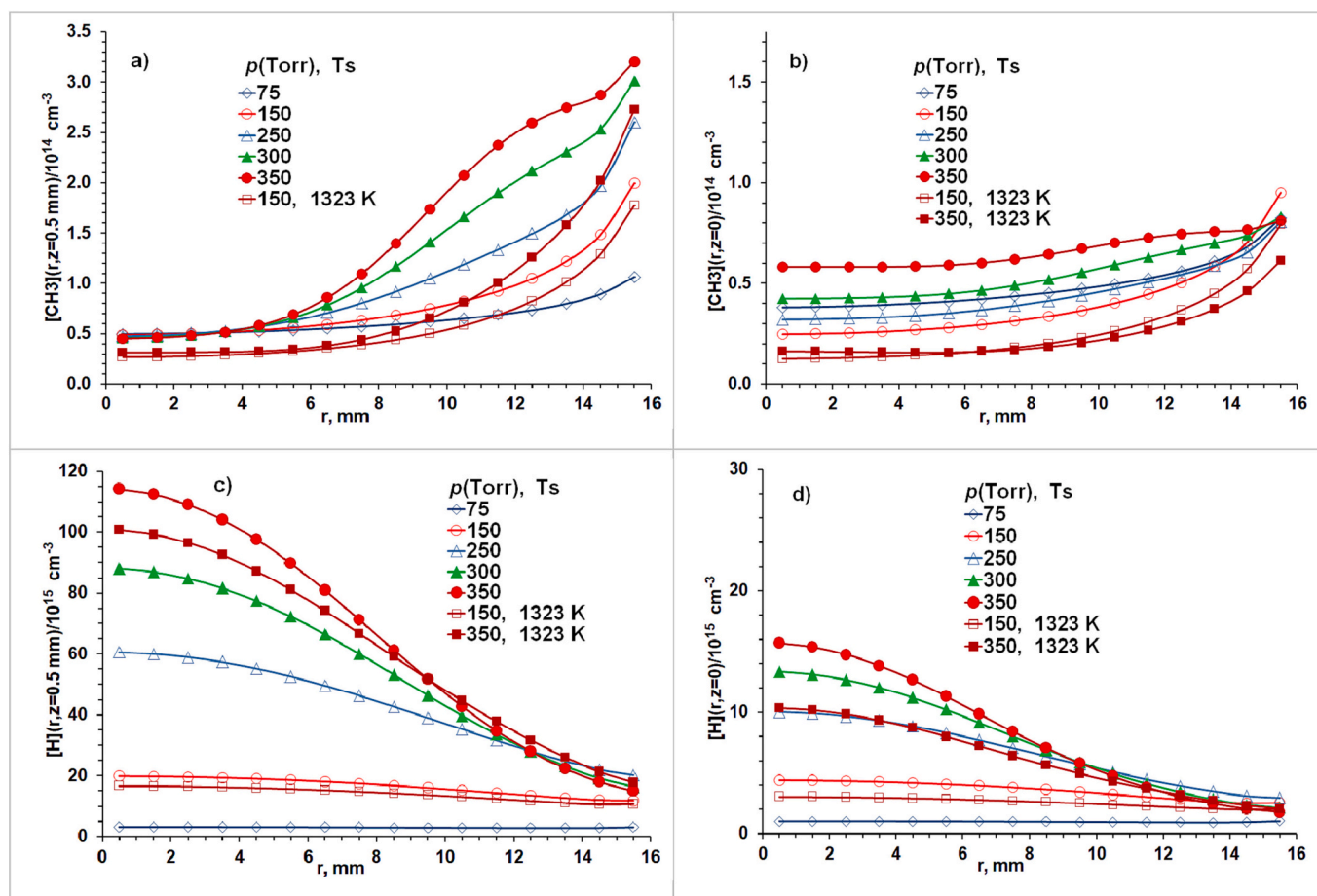


Fig. 7. Calculated (a) $[\text{CH}_3](r, z = 0.5 \text{ mm})$ and (c) $[\text{H}](r, z = 0.5 \text{ mm})$ distributions in a MW activated 0.006% N_2 /1% CH_4/H_2 gas mixture at various pressures in the range $75 \leq p \leq 350$ Torr, with $P = 1.4$ kW and $T_s = 1073$ K, and for two additional regimes with $T_s = 1323$ K. Panels (b) and (d) show the corresponding radial profiles immediately above the substrate surface ($z = 0$). Note the different y-axis scales used for the $z = 0.5$ mm and $z = 0$ mm traces for each species.

weaker p dependence ($[\text{CH}_{3\text{max}}] \sim p^{0.8}$). The maximal gas temperature, T_{gmax} , also progressively increases with p , from 2985 K at $p = 75$ Torr, through 3196 K at 150 Torr, to 3430 K at 350 Torr. The radial profiles of T_{g} just above the substrate are rather uniform at low p but become increasingly non-uniform at higher p – inducing predictable trends for the species radial distributions. These trends are illustrated in Figs. 7(a) and 7(c), which show, respectively, the CH_3 radical and H atom radial distributions at $z = 0.5$ mm returned by the 2D modeling for $P = 1.4$ kW and $T_{\text{s}} = 1073$ K. The $[\text{H}](r)$ distributions become increasingly non-uniform at higher p , with the greatest increases at $r \sim 0$. The $[\text{CH}_3](r)$ distributions are also non-uniform, showing a more complex p -dependence with the largest increases at $r \gg 0$. Fig. 7(b) and (d) show the corresponding distributions at $z = 0$, estimated using the approach described in Section 2.6.

2.3. Effects of varying the absorbed power on the CH_3 radical and H atom distributions

Changes in P induce quite different trends in the plasma parameters (Fig. 2) and the species distributions, particularly those for the CH_3 and H atoms. For $p = 150$ Torr, Fig. 8 shows the 2D distributions of these species calculated for $P = 1$ and 3 kW. (The $[\text{CH}_3]$ distribution for $P = 1.4$ kW was shown in Fig. 5(a)). The H atom distribution expands with increasing P , as does the width of the zone B of maximal CH_3 concentration. $[\text{H}_{\text{max}}]$ and $[\text{CH}_{3\text{max}}]$ both increase weakly with P , i.e. $[\text{H}_{\text{max}}] \sim P^{0.4}$ and $[\text{CH}_{3\text{max}}] \sim P^{0.45}$. The maximal gas temperature T_{gmax} declines gently with increasing P , from $T_{\text{gmax}}(1 \text{ kW}, 150 \text{ Torr}) \sim 3200$ K down to $T_{\text{gmax}}(3 \text{ kW}, 150 \text{ Torr}) \sim 3140$ K. As noted above, the maxima of n_e , T_e (Fig. 2) and T_{g} at high power ($P = 3$ kW) are all in the region above the substrate edge (at $r \sim 1.6$ cm) whereas, at lower powers ($P \leq 1.4$ kW), these maxima fall in the axial region (at $r = 0$). That dn_e/dr , dT_e/dr and dT_{g}/dr all display positive gradients above the substrate at high P improves the uniformity of the radial profile of $[\text{H}]$ with increasing P (Figs. 8 and 9(c), for constant $p = 150$ Torr and $T_{\text{s}} = 1073$ K). The $[\text{CH}_3](r)$ profiles at $z = 0.5$ mm (Fig. 9(a)) also become more uniform at higher P , though the effect is less dramatic. The corresponding radial profiles after extrapolation to $z = 0$, shown in Fig. 9(b) and (d), are discussed further in Section 2.6. As these figures show, the predicted $[\text{CH}_3]$ and

$[\text{H}]$ values above the substrate center ($r \sim 0$) are only weakly P -dependent, whereas $[\text{H}]$ above the substrate edge is found to increase faster than linearly with increasing P .

2.4. Effects of varying substrate temperature on the CH_3 radical and H atom distributions

Additional traces in each panel of Fig. 7 show the calculated $[\text{CH}_3](r)$ and $[\text{H}](r)$ profiles at $z = 0.5$ mm and, after extrapolation, at $z = 0$ in the same MW activated 0.006% N_2 /1% CH_4 / H_2 mixture operating at two pressures ($p = 150$ and 350 Torr), $P = 1.4$ kW and a higher substrate temperature, $T_{\text{s}} = 1323$ K. Relative to the corresponding data for $T_{\text{s}} = 1073$ K, the 2D calculations show that raising T_{s} reduces both $[\text{CH}_3]$ and $[\text{H}]$ in the near substrate region. This can be traced to the higher loss probability for H atoms at the growing diamond surface (γ_{H}) (~ 0.134 at $T_{\text{s}} = 1323$ K, cf. ~ 0.094 at $T_{\text{s}} = 1073$ K) [44] which encourages $[\text{H}]$ loss as $z \rightarrow 0$. The reduced H atom concentration reduces the probability of converting C_2H_2 to CH_4 in zones B and C, which manifests in lower near surface $[\text{CH}_4]$ and $[\text{CH}_3]$ values at higher T_{s} . Higher T_{s} inevitably implies higher T_{g} and, thus lower total number density (at any fixed p). This decline is further exacerbated in the case of the hydrocarbon species by thermodiffusional transfer, which ensures a further reduction in the carbon balance in the near substrate region at higher T_{s} ($X(\text{C}) \sim 0.58$ % for $T_{\text{s}} = 1323$ K vs. ~ 0.67 % for $T_{\text{s}} = 1073$ K, cf. 1 % for the input gas mixture).

Discussion of the effects of d_{s} on the radial distributions of $[\text{H}]$ and $[\text{CH}_3]$ near the growing diamond surface and thus on the growth rate G are reserved for Section 3.3.

We end these sections by stressing that, though all these calculations are for a 0.006% N_2 /1% CH_4 / H_2 gas mixture, the 60 ppm of N_2 has no significant effect on the EEDF, the plasma parameters or the C_yH_x concentrations (cf. an N-free 1% CH_4 / H_2 mixture). The effects of N_2 additions on the plasma parameters and species concentrations were reported recently for the case of a MW activated 0.6% N_2 /4% CH_4 / H_2 gas mixture [3]. Even for this much higher N_2 fraction (6000 ppm, cf. the 60 ppm of current interest), N-containing ions (principally HCNH^+ , NH_4^+ , N_2H^+) were predicted to contribute no more than 1 % of the total ion content in the hot plasma core (and only ~ 4 % of the total ion content

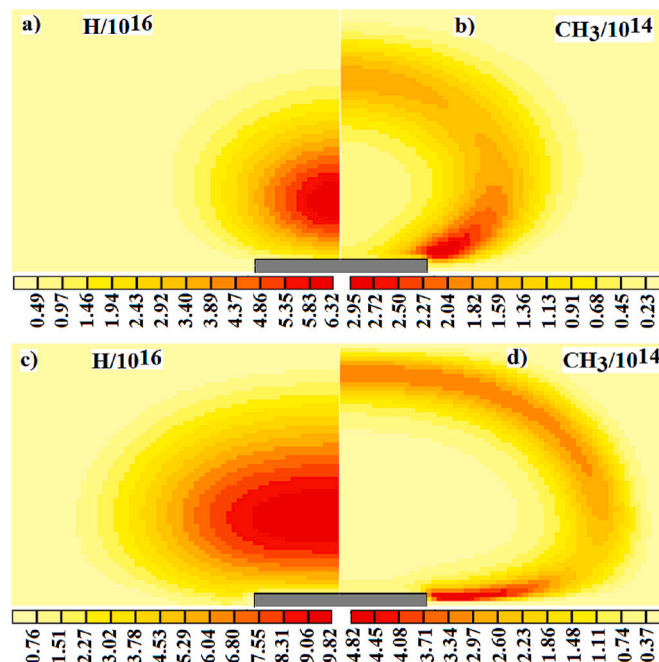


Fig. 8. Calculated 2D(r, z) distributions of (a) and (c) H atom concentrations and (b) and (d) CH_3 radical concentrations in a MW activated 0.006% N_2 /1% CH_4 / H_2 gas mixture at $p = 150$ Torr, with $P = 1$ kW (panels (a) and (b)) and 3 kW (panels (c) and (d)). All other details are as for Fig. 1.

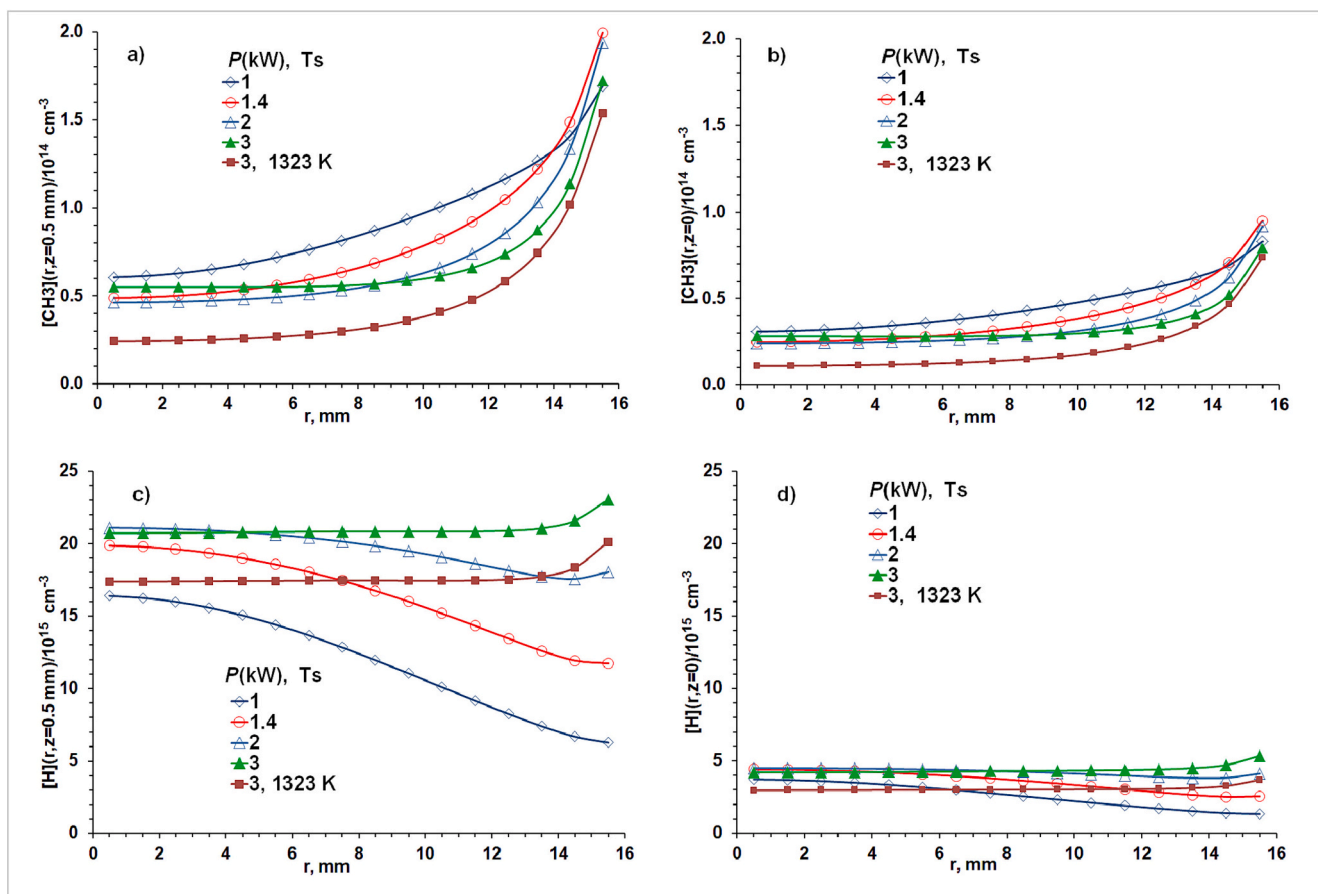


Fig. 9. Calculated (a) $[\text{CH}_3](r, z = 0.5 \text{ mm})$ and (b) $[\text{H}](r, z = 0.5 \text{ mm})$ distributions in a MW activated 0.006% N_2 /1% CH_4 / H_2 mixture at various absorbed powers in the range $1 \leq P \leq 3$ kW, with $p = 150$ Torr and $T_s = 1073$ K. Panels (b) and (d) show the corresponding radial profiles immediately above the substrate surface ($z = 0$).

just above the substrate), and the addition of trace amounts of N_2 was shown to induce no discernible changes in the plasma parameters (n_e , T_e , T_g , reduced electric fields) or the C_yH_x species concentrations, as can be seen, for example, from rows 6, 7 and 9 in Table 3 of Ref. [3].

2.5. Principal differences between 1D and 2D modeling

The data shown in Figs. 1-9 illustrate the fundamentally two-dimensional spatial distributions of the plasma parameters and species concentrations and the complex picture of hydrocarbon interconversions throughout the whole reactor, i.e. the main problems associated with attempting to use 1D models to describe PACVD reactors. As can be seen from the 2D plots, the radial and axial gradients associated with diffusional/thermodiffusional transfer in the r and z directions are broadly comparable. Calculations of C_yH_x axial concentration profiles in a 1D($z, r = 0$) model cannot accommodate any radial transfers and neglect important conversions in off-axial regions. Similarly, any radial 1D(r) model cannot allow for axial transfers and important axially varying conversions. Further, there is no accurate procedure for setting boundary conditions in 1D(z) and 1D(r) models, e.g. species concentrations at the upper boundary (near the quartz window) for a 1D(z) model or near the walls of the cylindrical reactor for a 1D(r) model where, as Fig. 5 showed, the gas mixture is very different from the initial CH_4/H_2 input mixture (with or without trace N_2 additions).

These problems are well illustrated by the quantitatively different trends predicted by the previous 1D(z) model developed for, and applied to, the Gicquel group reactor [6,45] and by the present 2D(r, z) modeling for the relationship between the CH_3 concentration just above the substrate center and the maximal H atom concentration in the plasma core, $[\text{H}_{\text{max}}]$, in plasmas operating with the same $X(\text{CH}_4) = 4\%$, $d_s = 50$ mm and $T_s = 1123$ K and a range of different p and P . Fig. 10 shows four data sets, each plotted as a function of $[\text{H}_{\text{max}}]$, where the $[\text{H}_{\text{max}}]$ values are from two sources: experimental estimates from OES/actinometry measurements (green points [6]) and the present 2D(r, z) modeling for the specified p and P conditions (all other points). The agreement between the experimental and predicted $[\text{H}_{\text{max}}]$ values derived for similar conditions (e.g. for $p \sim 150$ Torr, $P = 3$ kW or for $p \sim 200$ Torr, $P = 3.5$ kW) is reassuring. The four displayed data sets are, respectively, $[\text{CH}_3](r = 0, z = 0.5 \text{ mm})$ values returned by the 2D(r, z) model, $[\text{CH}_3](r = 0, z = 0)$ and $[\text{H}](r = 0, z = 0)$ values obtained by extrapolating the corresponding $r = 0, z = 0.5 \text{ mm}$ values as described in Section 2.6, and the $[\text{CH}_3](z = 0)$ values returned by the earlier 1D(z) calculations [6]. Whilst not excluding the possibility that there might be some reactor specific reasons for such very different predicted trends in $[\text{CH}_3](z = 0)$ vs $[\text{H}_{\text{max}}]$, the limited available data suggest that similarities (i.e. reactor independent trends) are more likely – as found, for example, when comparing the p -dependent $I(\text{C}_2^*)/I(\text{H}_\alpha)$ ratio returned by different reactors [12].

Thus, the difference between the 1D model prediction that $[\text{CH}_3](z$

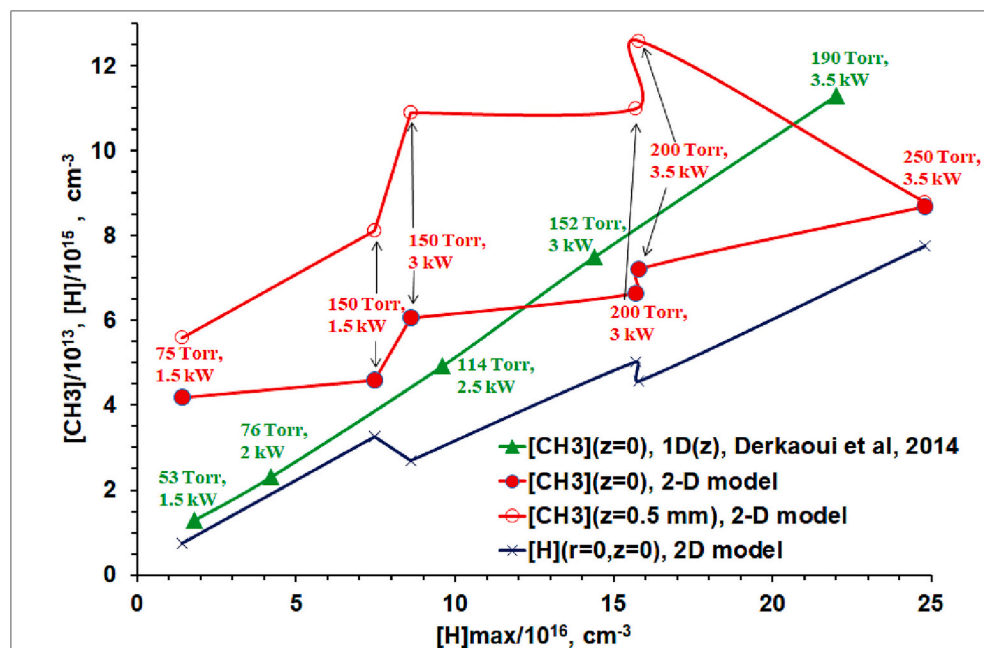


Fig. 10. CH₃ concentration above the substrate center ($r = 0$) plotted against the maximal H atom concentration, $[H]_{\max}$, calculated for a 0.006%N₂/4%CH₄/H₂ gas mixture, $d_s = 50$ mm and $T_s = 1123$ K by (i) the present 2D(r, z) model (red open circles for $z = 0.5$ mm, red filled circles after 1D extrapolation to $z = 0$) and (ii) the 1D(z) model reported in refs. 6 and 45 (green triangles), for regimes involving various p and P (defined alongside the various data points as p , Torr, P , kW). The $[H](r = 0, z = 0)$ values returned by the present calculations are also shown to illustrate their linear variation with $[H]_{\max}$.

$= 0$) increases near-linearly with $[H]_{\max}$ and the much shallower dependence returned by the present 2D modeling is noteworthy, and should sound a cautionary note when considering the application of 1D models to describe the manifestly 2D nature of PACVD reactors. A 1D model, for example, could not properly capture a dependence of $[CH_3]$ ($z = 0$) (and thus the growth rate) on substrate diameter, which the present 2D modeling predicts to be significant, particularly at low pressures: e.g. $[CH_3](r = 0, z = 0) = 5.5 \times 10^{13}$ and 4.2×10^{13} cm⁻³ for $d_s = 32$ and 50 mm, respectively, at $p = 75$ Torr and $P = 1.5$ kW. The more complex (i.e. not simple linear) variation of $[CH_3](z = 0)$ with $[H]_{\max}$ (and thus with $[H](z = 0)$, given the proportionality $[H](z = 0) \sim 0.03 \times [H]_{\max}$ in Fig. 10) is unsurprising, given the contributions from reactions involving CH₄ and C₂H₅ (Eq. (4) and Table 1), the concentrations of both of which also depend on many factors [19,20] in addition to $[H]$.

2.6. Use of a 1D(z) model to extrapolate dependencies in the boundary region ($z < 0.5$ mm)

Notwithstanding these reservations, there are instances where the computational effort of 2D calculations becomes disproportionate and pragmatic 1D modeling may be appropriate. Such 1D(z) modeling for various r may well be appropriate if confined to the thin boundary layer $0 \leq z \leq z_b$ just above the substrate, where the steep gradients in T_g and the various species concentrations and axial transfer rates far exceed the corresponding radial gradients and transfer. Again, however, any such 1D(z) modeling requires appropriate boundary conditions at z_b (for a range of r). 2D modeling provides the obvious (and arguably the only) way of establishing adequate boundary conditions for the various species concentrations and for $T_g(r, z_b)$.

Such a 1D(r_i, z) approach has been used here, using the 2D modeling results at $r_i, z_b = 0.5$ mm (from calculations using grid cell dimensions $\Delta z = 1$ mm and $\Delta r = r_{i+1} - r_i = 1$ mm) as the boundary conditions, to gain a more detailed picture of the sharp variations in the various C_{*y*}H_{*x*} species concentrations in the boundary layer above the substrate and to

calculate $[CH_3](r_i, z = 0)$ and $[H](r_i, z = 0)$ values required for the estimation and analysis of diamond growth rates (Section 3). The methyl radical concentration at the substrate surface, $[CH_3](z = 0)$, is determined by the balance of reactions (1)–(3) and, to a lesser extent, by the rate of carbon incorporation at the surface. However, the C_{*y*}H_{*x*} concentrations and thus the rates of reactions (1)–(3) in the near substrate region are rapidly varying functions of z , because of the steep dT_g/dz and $d[H]/dz$ gradients and the ways in which these affect the various chemical transformations and diffusional and thermodiffusional transfers.

Additional 1D(r_i, z) calculations were therefore undertaken for the near substrate ($z = 0$ –0.5 mm) region to refine the behavior of the various $[C_yH_x]$. These recognize the temperature jump ΔT at the substrate

$$\Delta T = T_g(z = 0) - T_s \approx 2.4 \times ((1/\alpha_{H_2}) - 0.5) \times \lambda_{H_2} \times dT_g/dz, \quad (6)$$

where α_{H_2} and λ_{H_2} are, respectively, the thermal accommodation coefficient and mean free path of H₂ molecules [46]. For hot ($T > 1000$ K) surfaces, α is low (< 0.1) and the typical temperature jumps range between $\Delta T[K] \approx 5.6/\alpha_{H_2}$ for $p \leq 150$ Torr and $\Delta T[K] \approx 3.7/\alpha_{H_2}$ for $p = 350$ Torr under the conditions of current interest. Assuming $\alpha_{H_2} \approx \alpha_{He}/1.5 \approx 0.07$ [47], these jumps are in the range ~ 50 –100 K and thus sufficient to affect the T_g -dependent rate coefficients of reactions (1)–(3) and thus the $[CH_3](z)$ values near the substrate.

Fig. 11 illustrates the strong variations of the base species concentrations and of $T_g(r = 0, z)$ in the near substrate region for 0.006%N₂/ x %CH₄/H₂ gas mixtures under three different process conditions: (a) $x = 1, p = 150$ Torr, $P = 1.4$ kW and $T_s = 1073$ K (i.e. base conditions for the results shown in Section 2.1); (b) $x = 4, p = 150$ Torr, $P = 1.4$ kW and $T_s = 1123$ K; and (c) $x = 4, p = 250$ Torr, $P = 3.5$ kW and $T_s = 1123$ K (both of which conditions featured in Fig. 10). All three plots show an obvious increase in $[H_2]$ on approaching the substrate, reflecting the inevitable increase in total number density on moving to a region of lower T_g whilst maintaining constant p . Thermodiffusional transfer into the cooler near-substrate region ensures that the local

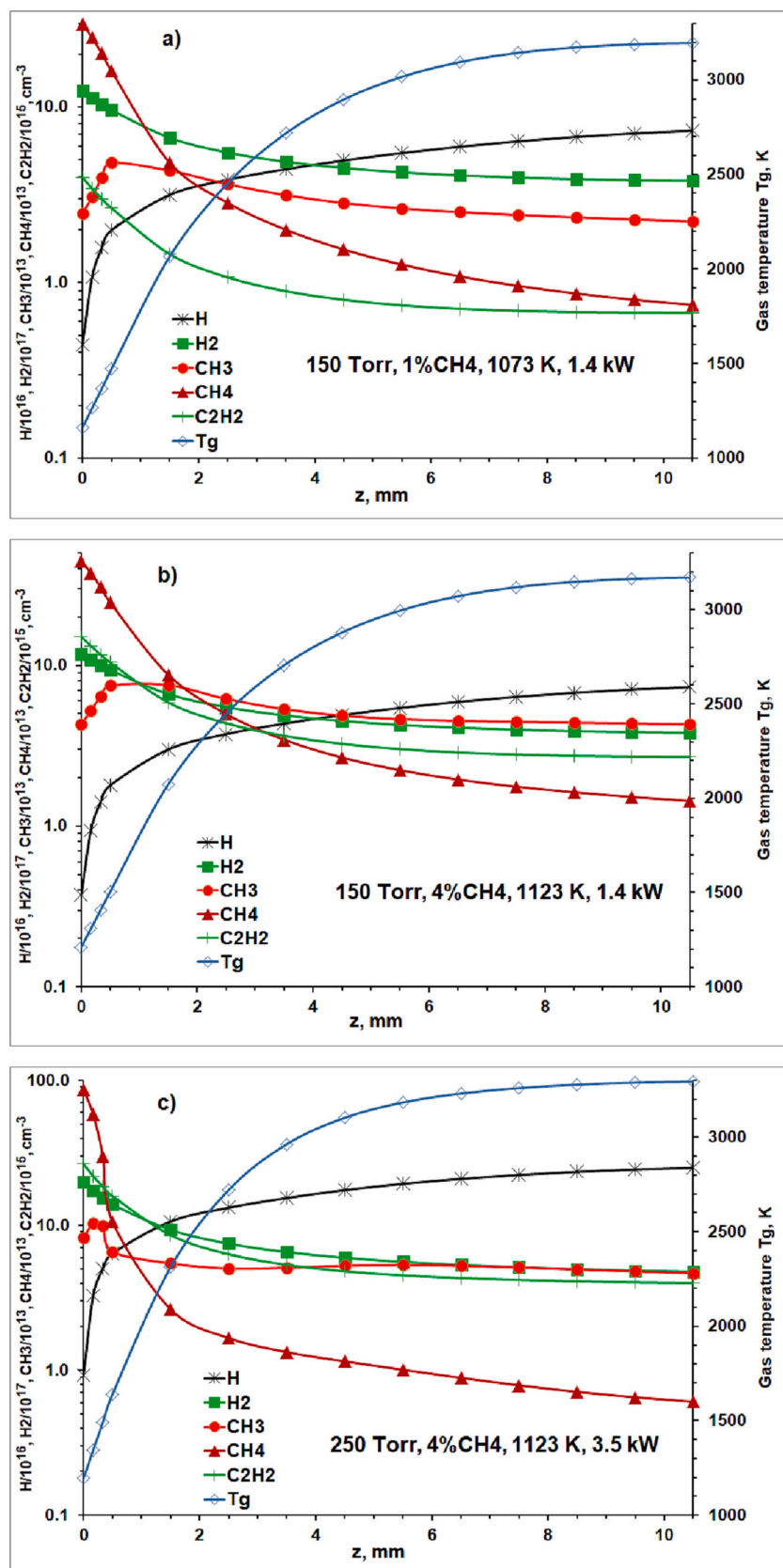


Fig. 11. Plots illustrating the steep z -dependent variations in $T_g(r=0, z)$ and in the concentrations of selected species in the near substrate region for $0.006\%N_2/x\%CH_4/H_2$ gas mixtures under three different process conditions: (a) $x = 1, p = 150$ Torr, $P = 1.4$ kW and $T_s = 1073$ K; (b) $x = 4, p = 150$ Torr, $P = 1.4$ kW and $T_s = 1123$ K; and (c) $x = 4, p = 250$ Torr, $P = 3.5$ kW and $T_s = 1123$ K. Data points for $z \geq 0.5$ mm are from 2D(r, z) calculations while those for $z < 0.5$ mm are from the 1D($r_1 = 0, z$) calculations described in Section 2.6.

carbon content (mainly determined by C_2H_2) increases more steeply than $[H_2]$ as $z \rightarrow 0$, but the near substrate $[CH_4]/[C_2H_2]$ ratio is significantly higher at the higher x (compare Fig. 11(a) and (b)) and increases more steeply as $z \rightarrow 0$ at higher p and P (compare Fig. 11(b) and (c)). $[H]$ decreases on approaching the substrate, as does $[CH_3]$ under most regimes studied. $[CH_3]$ shows the gentler (relative) decline due to a combination of thermodiffusional transfer effects and (indirectly) because of the increasing carbon balance. The current modeling returns $[CH_3](z=0) \sim [CH_3](z=0.5 \text{ mm})$ under high p , P conditions (250 Torr, 3.5 kW – see Figs. 10 and 11(c)). Reference to Table 1 shows that this can be traced to the much greater contribution from reaction (3), which yields two CH_3 radicals, under higher p , P conditions.

3. Diamond growth rates and their dependence on gas pressure, absorbed power, N_2 additions and the substrate temperature and diameter

3.1. Development of a growth rate expression

These calculated $[CH_3](z=0)$ and $[H](z=0)$ concentrations at the substrate surface along with a gas-surface reaction mechanism [48] allow the proposal of a semi-empirical growth rate formula $G_{\text{model}}([CH_3], [H], T_s, X(N_2))$ that can be normalized against experimental diamond growth rates, G_{exp} , measured under the same (or very similar) conditions. This modeling assumes the following reaction mechanism for CH_3 radical adsorption at relevant dimer radical (C^*) sites created and passivated by the H atom abstraction/addition reactions (7) and (8) [1,44,48,49]:



where all surface sites are designated in bold to distinguish them from gas phase species. Reactions (7) and (8) with rate coefficients k_7 , k_{-7} and k_8 from [48] provide an estimate of a dimer radical fraction.

$$F^* = 1/(1 + 0.3 \times \exp(3430/T_s) + 0.1 \times \exp(-4420/T_s) \times [H_2]/[H]) \quad (10)$$

To derive the G_{model} formula, we start from an upper estimate of the growth rate (G_{max}) under hypothetical conditions where every adsorbed CH_3 radical is assumed to be irreversibly incorporated into a diamond film:

$$G_{\text{max}} [\mu\text{m h}^{-1}] \approx 2 \times T_s^{0.5} \times ([CH_3]/10^{13}) \times F^* \times f \quad (11)$$

where the $[CH_3]$, $[H]$ and $[H_2]$ concentrations just above the substrate (i.e. at $z=0$) are in cm^{-3} and, in this limit, the incorporation probability, $f=1$. In reality, major uncertainties apply to the value of f , which can be viewed as the product of a sticking probability associated with reaction (9) and the probability of subsequent irreversible incorporation. Considering analogous gas phase radical-radical addition reactions (e.g. $CH_3 + CH_3 + M \rightarrow C_2H_6 + M$, with rate coefficient $k \sim (2-10) \times 10^{-30} \text{ cm}^6 \text{ s}^{-1}$ for the conditions of present interest and T_g in the range 1350–1000 K [50]) suggests a high sticking probability at typical substrate temperatures ($T_s = 1000-1200 \text{ K}$), though we also note the results of earlier molecular dynamics calculations which suggested sticking coefficients as low as ~ 0.1 for CH_3 radicals on bare (i.e. non-H-terminated) diamond (100) 2×1 and (111) 1×1 surfaces at these temperatures [51]. There are (at least) two pathways by which an incident CH_3 radical can proceed via CCH_3 in Eq. (9) to a surface CH_2 group: (i) chemisorption on a pure radical site C^* (with all adjacent surface atoms terminated as CH sites) followed by H abstraction by an

impinging gas phase H atom; and (ii) chemisorption at a biradical site C^{**} (i.e. a surface radical site with another nearby C^* site) followed by H atom transfer from the CCH_3 group to this adjacent site [1,36,49,52,53].

The surface CH_2 group deriving from an incident CH_3 radical can suffer a range of fates, including migrating on the diamond surface, being etched back into the gas phase (by incident H atoms) or ultimate incorporation into a diamond film (e.g. at a step edge) [1,49,52–58]. To develop the model further first requires some estimation of the fraction of adsorbed CH_3 groups that are further converted to surface CH_2 groups, migrate and ultimately incorporate into the growing diamond film. The fraction of migrating CH_2 groups that are etched in the period between initial accommodation and eventual irreversible incorporation must depend on process conditions, crystallite surface and sizes, etc., and the probability that the C atom in a chemisorbed CH_3 species (Eq. (9)) is irreversibly incorporated into growing diamond will have a complex dependence on many parameters. To complicate matters further, we recently proposed that incorporated N atoms might serve to immobilize adjacent CH_2 groups on the diamond surface and thereby facilitate growth of small islands that provide additional step-edges and encourage further incorporation and higher growth rates [3]. This picture is developed further in Section 4.

Many prior studies have shown that the presence of some nitrogen in the CH_4/H_2 process gas mixture (either via unintended air contamination or by specific controlled N_2 addition) can lead to enhanced diamond growth rates, to extents that depend on process conditions [26–34]. These observations and the foregoing concepts can be accommodated by stressing an $X(N_2)$ -dependent incorporation probability, henceforth designated as $f(X(N_2))$, and introducing $f(X(N_2))$ into the expression for G_{model} , i.e.

$$G_{\text{model}} = G_{\text{max}} \times f(X(N_2)) \approx 2 \times T_s^{0.5} \times ([CH_3]/10^{13}) \times F^* \times f(X(N_2)) \quad (12)$$

where the factor $f(X(N_2)) \leq 1$ describes the ratio of successful carbon incorporations relative to all CH_3 radical – surface radical collision events (Eq. (9)).

$f(X(N_2))$ can be treated as an empirical, process-dependent factor that could be estimated by, for example, comparison of modeling and experimental results for the same PACVD regimes and gas mixtures. Such comparisons for the Bristol PACVD reactor operating at process parameters ($p = 150 \text{ Torr}$, $P = 1.4 \text{ kW}$, $T_s = 1038 \text{ K}$, $X(CH_4) \sim 4\%$ (the average mole fraction during the first 0.5 h of deposition in a zero gas flow study) in H_2 with a minimal (unintended) nitrogen mole fraction $X_{\text{min}}(N_2)$ of a few ppm at most) yielding a measured polycrystalline diamond growth rate $G_{\text{exp}} \sim 1.4 \mu\text{m h}^{-1}$ on a $10 \times 10 \text{ mm}^2$ silicon substrate [59] return values of $[CH_3](z=0) \sim 6.5 \times 10^{13} \text{ cm}^{-3}$ (cf. $\sim 10^{14}$ at $z = 0.5 \text{ mm}$) – averaged over the substrate area – and

$$f(X_{\text{min}}(N_2)) \approx 0.03 \quad (13)$$

A similar calculation for $T_s = 1153 \text{ K}$ and $G_{\text{exp}} \sim 1.8 \mu\text{m h}^{-1}$ [59] returns a value $f(X_{\text{min}}(N_2)) \sim 0.05$, i.e. this approach would suggest that ~ 1 in 25 CH_3 species that impinge on a C^* radical site are ultimately incorporated into the diamond film under these practically N-free growth conditions. This leaves open the possibility of a significantly higher G at optimal nitrogen mole fraction $X_{\text{opt}}(N_2)$; the maximum possible increase in G by introducing an optimum amount of nitrogen would be limited by the factor $f(X_{\text{opt}}(N_2))/f(X_{\text{min}}(N_2))$, which would likely be process condition and sample dependent.

Derkaoui et al. reported near constant growth rates at $p \leq 150 \text{ Torr}$ (Fig. 10(a) in ref. 6). Given $G \sim [CH_3](z=0)$ (Eq. (12)), this observation correlates much better with the mildly varying $[CH_3](z=0)$ values predicted by the current 2D(r, z) modeling than with the 1D model

prediction [6] that $[CH_3]$ increases linearly with $[H_{max}]$ (Fig. 10). $f(X(N_2))$ values in a range 0.1 ± 0.025 can be obtained from the G and $[CH_3]$ data reported in that study, suggesting that addition of an optimal amount of N_2 could have afforded, at most, a ~ 10 -fold enhancement in G under the prevailing conditions. Under similar reactor conditions, Achard et al. actually reported a 10-fold enhancement in the growth rate of homoepitaxial single crystal diamond when adding 200 ppm N_2 to a MW activated 4% CH_4 in H_2 gas mixture operating at PD $\sim 95 W cm^{-3}$ [30]. They also noted a change in growth mode, from step flow (identified by classical step bunching phenomena and the appearance of macro-steps) at low nitrogen concentrations to a bidimensional nucleation mode and no observable macro-steps at high $X(N_2)$.

Bogdanov et al. reported similar increases of G (by factors of ~ 6 at PD $\sim 40 W cm^{-3}$ and ~ 14 for PD $\sim 110 W cm^{-3}$) in the case of polycrystalline films grown on Si substrates when using their optimal nitrogen addition $X_{opt}(N_2) \sim 200$ ppm, cf. an N-free CH_4/H_2 plasma with $X(N_2) < 1$ ppm [27]. Even 50 ppm N_2 additions in the latter study were shown to result in ~ 5 -fold increases of G at both power densities. The smaller increases in G reported in some other studies upon adding

N_2 into a C_yH_x/H_2 mixture could have arisen if the nominally N-free 'base' mixture actually contained some unintended N_2 fraction (e.g. from process gas contamination and/or air leakage into the reactor).

3.2. Effects of changing substrate temperature

As noted above, the value of $f(X(N_2))$ in the growth expression (Eq. (12)) will depend on many factors, including process conditions and the morphology of the growing surface. In general, process regimes with higher $[H](z=0)$ should be expected to suppress $f(X(N_2))$ values due to H-induced etching of migrating CH_2 groups. Conversely, increasing $X(N_2)$ can demonstrably result in higher $f(X(N_2))$ values. It can be expected that variations in $f(X(N_2))$ values and $[CH_3]/[H](z=0)$ ratios will affect the quality of the deposited material.

The illustrative examples in the remainder of this Section are all for the base 0.006% $N_2/1\%CH_4/H_2$ gas mixture and assume a value $f(X(N_2)) = 0.03$. Under these conditions, Eq. (12), with constant $T_s = 1073 K$, returns growth rates at the substrate center in the range $0.5 <$

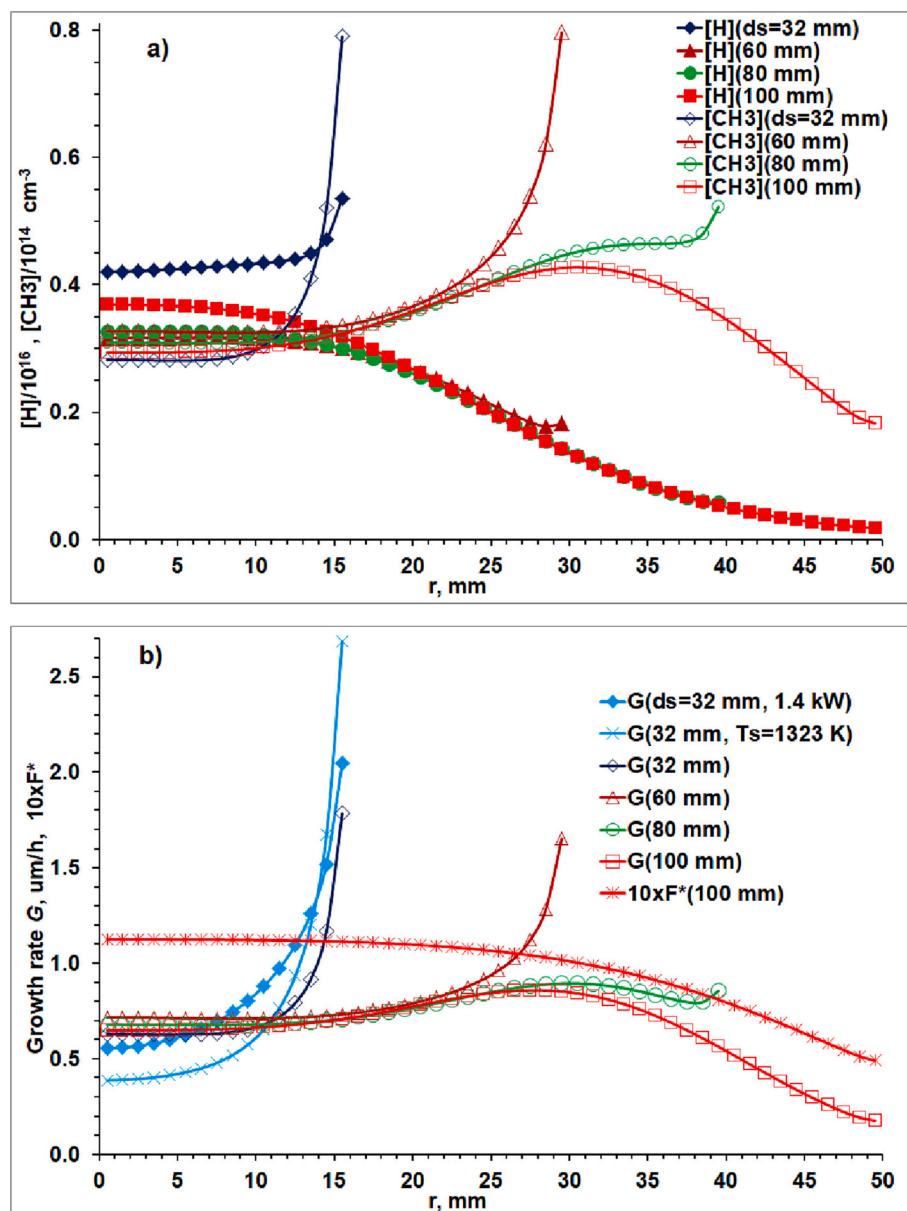


Fig. 12. Radial profiles of (a) $[H](r, z=0)$ and $[CH_3](r, z=0)$ and (b) G (from Eq. (12) with the factor $f(X(N_2)) = 0.03$) for various substrate diameters $d_s = 32, 60, 80$ and 100 mm, with $p = 150$ Torr, $P = 3$ kW and $T_s = 1073$ K. Three further plots are shown in panel (b). One shows the F^* profile (scaled by a factor of 10) for $d_s = 100$ mm under these conditions to illustrate the ~ 2 -fold decline in F^* at large r , while the other two (light blue) curves illustrate the effects on $G(r)$ of (i) increasing T_s from 1073 to 1323 K while maintaining $P = 3$ kW and (ii) decreasing P from 3 to 1.4 kW while maintaining $T_s = 1323$ K, with $p = 150$ Torr and $d_s = 32$ mm in both cases.

$G_{\text{model}}/(f(X(N_2))/f(X_{\text{min}}(N_2))) < 1.3 \mu\text{m h}^{-1}$, for a broadly constant $F^* \sim 0.11$ (from Eq. (11)) and respective methyl concentrations in the range $2.5 \times 10^{13} < [\text{CH}_3](r=0, z=0) < 5.9 \times 10^{13} \text{ cm}^{-3}$ for the spread of p and P conditions considered in Figs. 7 and 9. As Fig. 12(b) shows, G is predicted to maximize near the substrate edge. For this small substrate size ($d_s = 32 \text{ mm}$), the predicted increase in $[\text{CH}_3]$ under base conditions ($p = 150 \text{ Torr}$, $P = 1.4 \text{ kW}$, $T_s = 1073 \text{ K}$) more than outweighs the gentle decline in $[\text{H}]$ with increasing r (Fig. 7(d)). Note, the predicted $[\text{CH}_3]/[\text{H}]$ ratio at $z = 0$ increases from ~ 0.006 to ~ 0.04 (i.e. by a factor of ~ 7) as r increases from 0 to $d_s/2$ (16 mm), so the deposited material quality would likely show an r dependence. A second G vs r plot in Fig. 12(b) shows a similar r dependence at higher T_s (1323 K, whilst maintaining $p = 150 \text{ Torr}$ and $P = 1.4 \text{ kW}$). Such an increase in T_s is predicted to reduce $G(r=0)$ but to increase $G(r=d_s/2)$; a ~ 5 -fold increase in the $[\text{CH}_3]/[\text{H}](z=0)$ ratio is predicted in this case (from ~ 0.004 to ~ 0.02) and, again, the caveat about r -dependent material quality must apply. Increasing T_s (while holding all other process conditions fixed) changes the CH_3 balance (reactions (1)–(3) in Table 1) and results in lower $[\text{CH}_3]/[\text{H}](z=0)$ ratios. The evident r dependence of the $[\text{CH}_3]/[\text{H}](z=0)$ ratio under any given process conditions suggests that any more sophisticated growth model must recognize that $f(X(N_2))$ is also likely to be r dependent.

In experiments such as those reported in ref. 59, the (near-)constancy of T_s in the various p and P regimes (and thus at the various powers loadings to the substrate) could be achieved using an annular wire spacer of user-selectable diameter to hold the substrate off the water-cooled base-plate of the reactor. In alternative regimes employing a constant spacer wire thickness (i.e. constant gas gap), increasing p and/or P would change the power loading to the substrate (due to both heat conduction from the hot plasma and H atom accommodation at radical surface sites [39]) and thus change T_s accordingly, as described in ref. [3]. For very high T_s (e.g. $>1500 \text{ K}$), Eq. (11) can be modified to allow for thermal desorption of CH_3 (reaction (–9)) [60,61]. Other modifications of the growth rate formula to accommodate possible adsorption of CH_x ($x = 0\text{--}2$) radicals and of CH_3 radicals on dimer biradical sites have been presented also [48,60].

3.3. Effects of changing substrate diameter

Section 3.1 offers a kinetic description of how the nitrogen in a MW activated N/C/H gas mixture can lead to increased diamond growth rates, G , defined in terms of thickness per unit time. In some instances, the measurable of interest might be the volume (or mass) of diamond grown per unit time, and one obvious way of increasing the latter would be to increase the area over which deposition occurs. Fig. 2b and c illustrated how the n_e and T_e distributions change upon increasing the substrate diameter from $d_s = 32 \text{ mm}$ to 100 mm . Fig. 12 shows the calculated effects of d_s on the radial profiles of (a) $[\text{H}]$ and $[\text{CH}_3]$ at $z = 0$ and (b) G (in $\mu\text{m hr}^{-1}$). Base conditions of $p = 150 \text{ Torr}$, $P = 3 \text{ kW}$ and $T_s = 1073 \text{ K}$ were chosen for these comparisons, with d_s values of 32, 60, 80 and 100 mm . The $[\text{H}](z=0)$ profile is predicted to be relatively flat for $d_s = 32 \text{ mm}$ at this higher P , maximizing at $r = d_s/2 = 16 \text{ mm}$ (as in the 2D($r, z = 0.5 \text{ mm}$) data shown in Fig. 9), but for all larger d_s values $[\text{H}](z=0)$ is predicted to maximize at $r = 0$ and to fall fairly monotonically out to the substrate edge. $[\text{CH}_3](z=0)$ is predicted to maximize at $r = d_s/2$ for all but the largest diameter ($d_s = 100 \text{ mm}$).

The competing r dependences of $[\text{H}]$ and $[\text{CH}_3]$ at the substrate surface determine the predicted $G(r)$ profiles shown in Fig. 12(b) though, at larger d_s , the r dependence of F^* can no longer be ignored. For illustration, Fig. 12(b) also shows the $F^*(r)$ profile for $d_s = 100 \text{ mm}$ under these conditions: the ~ 2 -fold drop of F^* near the substrate edge can be traced to contributions from reaction (–7) at low $[\text{H}](r, z=0)$ and its effect on the last term in Eq. (9). As Fig. 12(b) shows, the predicted growth rates at $r \sim 0$ are largely insensitive to d_s but the d_s dependences of $\text{CH}_3(r, z=0)$ are clearly reflected in $G(r)$, which is still predicted to peak at the substrate edge when $d_s = 60 \text{ mm}$, but then to

maximize at $r \sim 30 \text{ mm}$ for $d_s \geq 80 \text{ mm}$.

Angular integration of these predicted $G(r)$ values over all r suggests that $\sim 6.5 \times$ more material would be deposited under the specified conditions per unit time when using a substrate with $d_s = 100 \text{ mm}$ (cf. $d_s = 32 \text{ mm}$) but, again, we note the very different $[\text{CH}_3]/[\text{H}](z=0)$ ratios at the substrate edge and center (which vary by factors of 13 (2.2) when $d_s = 100$ (32) mm) and caution that such large differences in gas phase composition would likely lead to r -dependent material quality and r -dependent $f(X(N_2))$ values – for which the present calculations make no allowance. (The calculated $[\text{CH}_3]/[\text{H}](z=0)$ ratios under these higher P conditions increase between $r = 0$ and $r = d_s/2$ from 0.007 to 0.015 for $d_s = 32 \text{ mm}$, from 0.01 to 0.044 for $d_s = 60 \text{ mm}$, from 0.009 to 0.09 for $d_s = 80 \text{ mm}$ and from 0.008 to 0.1 for $d_s = 100 \text{ mm}$). The modeling also assumes constant T_s across the entire substrate diameter, which may be hard to realize experimentally given the finite size of the hot plasma volume (Fig. 3) and the decline in $[\text{H}](z=0)$ at large r (Fig. 12(a)). The predicted decrease in the conductive contribution to substrate heating between $r = 0$ and $r = d_s/2$ is $< 25 \%$ for $d_s = 32 \text{ mm}$ but approaches a factor of 7 when $d_s = 100 \text{ mm}$. Such non-uniformities will be largely mitigated by fast radial heat conduction through the substrate, however, particularly given the relatively thick substrate holders used in most MW PACVD reactors.

4. Mechanism of N-induced growth rate enhancement

As noted earlier, a mechanistic interpretation of how and why trace amounts of nitrogen accelerate the rate of CVD diamond growth has been a topic of longstanding interest. Optical diagnoses of MW activated N/C/H plasmas have established N atoms as the most abundant potentially reactive N-containing species just above the growing diamond surface [2], and companion 2D(r, z) modeling has shown that trace additions of N_2 have minimal effect on the plasma parameters and the near-surface H atom or C_yH_x species concentrations [3]. Oberg et al. [36] recently summarized many model studies that have sought to explore ways in which sub-surface N atoms or N-containing adsorbate species might enhance growth rates by reducing reaction and/or transition state energies for growth on an H-terminated (100) surface [62–68], and showed (using density functional theory) the much reduced energy requirements for C insertion into a surface C–N dimer bond (cf. into the surface C–C dimer bond implicated in the accepted model for such C insertion [1]). These authors also reported energetically feasible reaction sequences leading to new layer growth propagating from the surface-embedded N atom and suggested that such surface C–N dimer bonds might serve as ‘super-nucleating’ species [55] capable of accelerating G in cases where new layer formation is the rate limiting step for growth. Such ideas chime with our recent suggestion

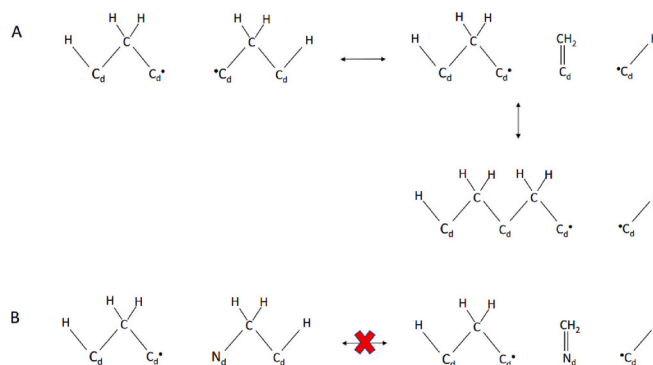


Fig. 13. A: Reaction pathway for migration of a pre-inserted CH_2 group to bridge a void in a chain of C-C dimer bonds on a (100)- 2×1 diamond surface. B: Analogous, energetically improbable, reaction sequence that would be required when one of the dimers contains a substitutional nitrogen atom.

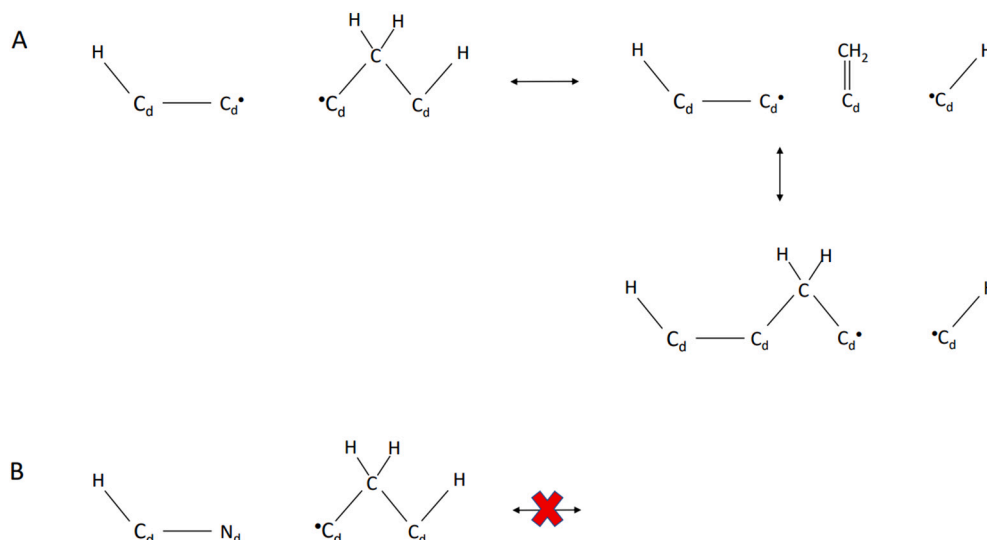


Fig. 14. Migration pathway of a CH₂ bridge group along a C-C dimer chain (A), and the improbable analogous reaction that would be required if approaching the N end of a C-N dimer (B).

that an incorporated N-atom (or small N-containing species) might serve as an anchor, immobilizing adjacent CH₂ groups on the diamond surface and thereby facilitating the formation of new, small islands that provide additional step-edges and encourage further incorporation [3]. These ideas are here outlined further.

Section 3.1 emphasized that the evolution from initial chemisorption of a CH₃ radical to irreversible C atom incorporation has a low success probability under typical diamond CVD conditions. Any picture of surface migration as a random walk process suggests short (few surface atom) net migration distances [49,56]. Growth models show a strong, energetically-driven propensity for eventual incorporation at step edges – consistent with observations of terraced surfaces and step-flow growth [1]. Most mechanistic studies focus on an idealised, flat, 2 × 1 reconstructed (100) diamond surface and build on the generally accepted model [69] wherein a CH₃ species attaches to a radical site on a C-C dimer bond and incorporates (as a bridging CH₂ group) via a successive ring-opening, ring-closing process. For eventual incorporation, this CH₂ group must migrate to a step edge, and several energetically feasible routes for migration along both dimer rows and dimer chains have been identified [52].

Fig. 13A shows one illustrative sequence (reaction 18 in ref. [49]) starting from two C-C dimer bonds, each after CH₂ insertion, separated by a void. Atoms in the surface dimer bonds prior to insertion are shown with a subscript d, and radical sites (dangling bonds) are indicated with a dot (•). In this depiction, the right hand CH₂ group migrates via a bond breaking, bond forming process via a transition state involving a pendant =CH₂ group leading to a bridge-next-to-bridge configuration, i. e., towards formation of a smooth surface. All steps are calculated to be energetically feasible at relevant substrate temperatures and the rate of this migration is predicted to be much (~2 orders of magnitude) faster than the rates of the H abstraction and addition reactions that control the surface radical population dynamics [49,52].

Fig. 13B depicts the analogous situation of two post-inserted dimer bonds, in one of which a C_d atom in the original dimer bond has been replaced by a substitutional nitrogen atom (N_d). The right-hand moiety in this case is the (H-terminated version of the) C-N dimer bond post CH₂ insertion, that Oberg et al. have shown to be stable [36]. The inability of the N_d atom to support a radical site ensures that CH₂ group migration

across the void (the analogue of Fig. 13A) will be blocked by the energetic penalty associated with trying to form the valency-defying N_d=CH₂ group. Post-insertion, therefore, the adjacent N_d atom serves to anchor the CH₂ group; it cannot migrate past the N_d atom. But that does not prevent further migration up to the anchored CH₂ group (as can be visualised by replacing the H terminated C_d atom in the left-hand structure in Fig. 13A with a substitutional N_d atom).

Similar arguments are likely to apply to other of the previously identified migration reactions. For example, Fig. 14A shows the migration of a CH₂ bridge group along a C-C dimer chain (reaction 20 in ref. [49]) that again will be prevented when approaching the N end of a C-N dimer (Fig. 14B).

In many regards, this analysis can be viewed simply as another perspective on a long-standing issue. The potential of an N_d atom to slow the propagation of a migrating step-edge and encourage step bunching was recognized long ago by van Enckevort and coworkers [70]. Oberg et al. focussed on the energetics of the sequence of elementary reactions resulting in CH₂ insertion into a C-N dimer bond and rearrangement reactions involving its immediate neighbours and noted that the N_d atom in this scenario has many of the attributes required of a ‘super-nucleating’ species [36]. The present analysis focusses more on surface migration efficiencies and the requirement of irreversible incorporation to achieve growth. The C-N dimer serves to lock an inserted CH₂ group, thereby offering a new nucleation or ‘anchor’ site on the surface. The N_d atom also acts as a barrier to the migratory passage of other CH₂ groups. Suitably immobilized, these CH₂ groups are ideally positioned to bond to the ‘anchor’ site and/or to pre-extended islands developing therefrom. The ‘catalytic’ effect of added nitrogen can thus be understood in terms of (i) creating additional, fixed, nucleation sites, which (ii) reduce the average migration distances needed to (iii) incorporate at the emerging step edges supported by such sites – thereby boosting the C incorporation probability relative to that prevailing under N-free conditions where more extensive surface migrations will typically be required.

5. Conclusions

Diamond deposition from MW plasma activated 0.006%N₂/1%CH₄/H₂ gas mixtures has been investigated by 2D(*r*, *z*) self-consistent

modeling, as functions of pressure ($p = 75\text{--}350$ Torr) and absorbed power ($P = 1\text{--}3$ kW), mostly at a fixed substrate temperature $T_s = 1073$ K and substrate diameter, $d_s = 32$ mm. The modeling elucidates a complex 2D picture of hydrocarbon interconversion throughout the whole reactor volume, revealing three main interconversion zones, comparable radial (r) and axial (z) gradients of the various species concentrations, and an annular shell-like $[\text{CH}_3](r, z)$ profile that reflects the spatial distribution of the main CH_3 radical source reaction, i.e. the rate of $\text{CH}_4 + \text{H} \leftrightarrow \text{CH}_3 + \text{H}_2$ reaction, for which the r - and z -gradients of the reactant species concentrations are diametrically opposite (Figs. 6–9). These results serve to highlight the challenge of using 1D(z) models to describe a complete MW PACVD reactor: 1D(z) models necessarily neglect any radial dependences and, for example, predict variations in CH_3 concentration above the substrate center, $[\text{CH}_3](r = 0, z)$, that are very different from those returned by the 2D modeling. At high pressures, the 2D modeling predicts substantial and contrasting radial gradients of $[\text{CH}_3]$ and $[\text{H}]$ above the substrate and a radially increasing diamond growth rate profile.

The 2D modeling traces the various pathways by which the absorbed MW power is partitioned and the main transformations/heat flows that follow (i.e. from the initially activated electrons, via rovibrational excitation of H_2 and C_2H_2 , collisional energy transfer leading to gas heating and eventual heat transfer to the reactor substrate and walls). The modeling reveals how the various plasma parameters (and the hot plasma volume, V_p) respond to changes in p and P . At fixed P , the maximal power densities, PD_{max} , and electron concentrations $n_{\text{e,max}}$ both increase with p ; V_p shrinks. In all regimes, the calculated $\text{PD}(r, z)$ distributions are non-uniform in both the radial and axial directions, which raise questions about the meaningfulness of the oft-quoted average power density quantity, PD_{aver} . The 2D modeling also reveals that PD_{aver} estimates based on experimental measurements of the glowing plasma volume (e.g. from the spatial distributions of C_2^* and/or H_α emissions) are likely to be significant overestimates of the real PD_{aver} ; a substantial part of the absorbed power ($\sim 30\%$ at $p = 150$ Torr) is shown to be absorbed in cooler regions outside the glowing plasma volume. At lower powers ($P \leq 1.4$ kW), the maximal values of n_e , T_e and the gas temperature, T_g , are all found above the centre of the substrate (i.e. at $r = 0$), but these maxima are all predicted to shift to above the substrate edge (i.e. at $r \sim 16$ mm for the $d_s = 32$ mm substrate) at high powers ($P = 3$ kW).

The plasma rearrangements and changes in plasma parameters upon varying p and P induce corresponding variations in the spatial distributions of the various species, including the radial concentration profiles of CH_3 radicals and H atoms just above the substrate. Upon increasing p , $[\text{CH}_3](z = 0)$ is predicted to increase most steeply at the substrate edge (i.e. at $r = d_s/2$), whilst $[\text{H}](z = 0)$ increases most steeply above the substrate center (i.e. at $r = 0$). $[\text{CH}_3](r = 0, z = 0)$ and $[\text{H}](r = d_s/2, z = 0)$ are found to vary only weakly with p at constant P . The spatial distributions of radical species (e.g. zone B in Fig. 5, which contains the maximal CH_3 concentrations) expand with increasing P (at constant p). $[\text{CH}_3]$ and $[\text{H}]$ above the substrate center are predicted to vary only weakly with P (again at constant p) and the radial profiles of $[\text{H}]$ become more uniform at higher P .

Spatial variations in the diamond deposition rate, G , are determined by the radial profiles of $[\text{CH}_3]$ and $[\text{H}]$ just above the substrate. Analyses of the various $G(r)$ profiles calculated for different p , P and, to lesser extent, T_s and d_s provide a basis for understanding and optimizing deposition regimes and rates. A previously proposed semi-empirical, process-parameter-dependent expression for G [48] is developed further to explicitly include the addition of N_2 to MW activated CH_4/H_2 gas mixtures and a new mechanistic picture presented to account for the observed N-induced enhancements in G . This picture requires surface embedded N atoms, which act as 'anchor' sites and offer a mechanism for

reduced CH_2 surface migration and more step-edges for irreversible incorporation of such migrating groups. Such a picture chimes with the concept of 'super-nucleation' sites [55] such as the recently recognized stable moiety formed by CH_2 insertion into a C-N dimer bond on the 2×1 reconstructed (100) diamond surface [36].

Declaration of competing interest

The authors declare that they have no known competing financial interests or personal relationships that could have appeared to influence the work reported in this paper.

Data availability

Data will be made available on request.

Acknowledgments

The work was performed within the Cooperation in Science and Technology Agreement between Lomonosov Moscow State University, Skobeltsyn Institute of Nuclear Physics, and the University of Bristol.

References

- [1] J.E. Butler, Yu.A. Mankelevich, A. Cheesman, J. Ma, M.N.R. Ashfold, Understanding the chemical vapor deposition of diamond: recent progress, *J. Phys. Condens. Matter* 21 (2009), 364201 (and references therein).
- [2] B.S. Truscott, M.W. Kelly, K.J. Potter, M.N.R. Ashfold, Yu.A. Mankelevich, Microwave plasma enhanced chemical vapour deposition of nitrogen doped diamond, II: $\text{CH}_4/\text{N}_2/\text{H}_2$ plasmas, *J. Phys. Chem. A* 120 (2016) 8537–8549.
- [3] M.N.R. Ashfold, Yu.A. Mankelevich, Self-consistent modeling of microwave activated $\text{N}_2/\text{CH}_4/\text{H}_2$ (and N_2/H_2) plasmas relevant to diamond chemical vapour deposition, *Plasma Sources Sci. Technol.* 31 (2022), 035005 (and references therein).
- [4] X.G. Li, J. Perkins, R. Collazo, R.J. Nemanich, Z. Sitar, Investigation of the effect of the total pressure and methane concentration on the growth rate and quality of diamond thin films grown by MPCVD, *Diam. Relat. Mater.* 15 (2006) 1784–1788.
- [5] K.W. Hemawan, T.A. Grotjohn, D.K. Reinhard, J. Asmussen, Improved microwave plasma cavity reactor for diamond synthesis at high-pressure and high-power density, *Diam. Relat. Mater.* 19 (2010) 1446–1452.
- [6] N. Derkaoui, C. Rond, T. Gries, G. Henrion, A. Gicquel, Spectroscopic analysis of H_2/CH_4 microwave plasma and fast growth rate of diamond single crystal, *J. Phys. D: Appl. Phys.* 47 (2014) 205201.
- [7] G. Lombardi, K. Hassouni, G.-D. Stancu, L. Mechold, J. Röpcke, A. Gicquel, Modeling of microwave discharges of H_2 admixed with CH_4 for diamond deposition, *J. Appl. Phys.* 98 (2005), 053303.
- [8] K. Hassouni, F. Silva, A. Gicquel, Modelling of diamond deposition microwave cavity generated plasmas, *J. Phys. D – Appl. Phys.* 43 (2010), 153001.
- [9] H. Yamada, A. Chayahara, Y. Mokuno, S. Shikata, Numerical microwave plasma discharge study for the growth of large single-crystal diamond, *Diam. Relat. Mater.* 54 (2015) 9–14.
- [10] E.J.D. Mahoney, A. Lalji, J.W.R. Allden, B.S. Truscott, M.N.R. Ashfold, Yu. A. Mankelevich, Optical emission imaging and modeling investigations of microwave activated SiH_4/H_2 and $\text{SiH}_4/\text{CH}_4/\text{H}_2$ plasmas, *J. Phys. Chem. A* 124 (2020) 5109–5128.
- [11] E.J.D. Mahoney, B.J. Rodriguez, S. Mushtaq, B.S. Truscott, M.N.R. Ashfold, Yu. A. Mankelevich, Imaging and modeling the optical emission from CH radicals in microwave activated C/H plasmas, *J. Phys. Chem. A* 123 (2019) 9966–9977.
- [12] J.P.P. Gore, E.J.D. Mahoney, J.A. Smith, M.N.R. Ashfold, Yu.A. Mankelevich, Imaging and modeling C_2 radical emissions from microwave plasma-activated methane/hydrogen gas mixtures: contributions from chemiluminescent reactions and investigations of higher-pressure effects and plasma constriction, *J. Phys. Chem. A* 125 (2021) 4184–4199.
- [13] V. Sedov, A. Martyanov, A. Altakhov, A. Popovich, M. Shevchenko, S. Savin, E. Zavedeev, M. Zhanaveskin, A. Sinogeykin, V. Ralchenko, V. Konov, Effect of substrate holder design on stress and uniformity of large-area polycrystalline diamond films grown by microwave plasma-assisted CVD, *Coatings* 10 (2020) 939.
- [14] A. Rifai, D. Creedon, N. Tran, M. Hejazi, D. Garrett, A.D. Greentree, E. Pirogova, A. Stacey, K. Fox, Highly uniform polycrystalline diamond coatings of three-dimensional structures, *Surf. Coat. Technol.* 408 (2021), 126815.
- [15] J.A. Cuenca, S. Mandal, E.L.H. Thomas, O.A. Williams, Microwave plasma modelling in clamshell chemical vapour deposition diamond reactors, *Diam. Relat. Mater.* 124 (2022), 108917.

- [16] L. Li, C.C. Zhao, S.L. Zhang, Q.R. Gong, X.H. Sun, M. Qian, Y. Hang, Simulation of diamond synthesis by microwave plasma chemical vapor deposition with multiple substrates in a substrate holder, *J. Cryst. Growth* 579 (2022), 126457.
- [17] W. Cao, Z.B. Ma, D. Gao, J. Wu, T. Zhang, H. Zhang, H.Y. Zhao, Q.M. Fu, The effects of self-assembling off-angles on the homoepitaxial lateral outward growth of single-crystal diamond, *Vacuum* 212 (2023), 111989.
- [18] D. Yang, L. Guo, B. Wang, S. Jin, J.Q. Zhu, M. Zhai, Hydrogen plasma characteristics in a microwave chemical vapor deposition chamber, *Mater. Sci. Eng. B* 292 (2023), 116422.
- [19] Yu.A. Mankelevich, M.N.R. Ashfold, J. Ma, Plasma-chemical processes in microwave plasma enhanced chemical vapour deposition reactors operating with C/H/Ar gas mixtures, *J. Appl. Phys.* 104 (2008), 113304.
- [20] J. Ma, A. Cheesman, M.N.R. Ashfold, K.G. Hay, S. Wright, N. Langford, G. Duxbury, Yu.A. Mankelevich, Quantum cascade laser investigations of CH₄ and C₂H₂ interconversion in hydrocarbon/H₂ gas mixtures during microwave plasma enhanced chemical vapor deposition of diamond, *J. Appl. Phys.* 106 (2009), 033305.
- [21] J. Ma, J.C. Richley, D.R.W. Davies, M.N.R. Ashfold, Yu.A. Mankelevich, Spectroscopic and modeling investigations of the gas phase chemistry and composition in microwave plasma activated B₂H₆/CH₄/Ar/H₂ gas mixtures, *J. Phys. Chem. A* 114 (2010) 10076–10089.
- [22] P.-N. Volpe, J.-C. Arnault, N. Tranchant, G. Chicot, J. Pernot, F. Jomard, P. Bergonzo, Boron incorporation issues in diamond when TMB is used as precursor: toward extreme doping levels, *Diam. Relat. Mater.* 22 (2012) 136–141.
- [23] J.E. Butler, A. Vikharev, A. Gorbachev, M. Lobaev, A. Muchnikov, D. Radishev, V. Isaev, V. Chernov, S. Bogdanov, M. Drozdov, E. Demidov, E. Surovegina, V. Shashkin, A. Davydov, H. Tan, L. Meshi, A.C. Pakpour-Tabrizi, M.-L. Hicks, R. B. Jackman, Nanometric diamond delta doping with boron, *Phys. Status Solidi (RRL)* 11 (2017) 1600329.
- [24] J. Ma, J.C. Richley, D.R.W. Davies, A. Cheesman, M.N.R. Ashfold, Yu. A. Mankelevich, Spectroscopic and modeling investigations of the gas phase chemistry and consumption in microwave plasma activated B₂H₆/Ar/H₂ gas mixtures, *J. Phys. Chem. A* 114 (2010) 2447–2463.
- [25] L.J. Rogers, K.D. Jahnke, M.W. Doherty, A. Dietrich, L.P. McGuinness, C. Müller, T. Teraji, H. Sumiya, J. Isoya, N.B. Manson, F. Jelezko, Electronic structure of the negatively charged silicon-vacancy center in diamond, *Phys. Rev. B* 89 (2014), 235101.
- [26] S. Jin, T.D. Moustakas, Effect of nitrogen on the growth of diamond films, *Appl. Phys. Lett.* 65 (1994) 403–405.
- [27] S. Bogdanov, A. Vikharev, A. Gorbachev, A. Muchnikov, D. Radishev, N. Ovechkin, V. Parshin, Growth-rate enhancement of high-quality, low-loss CVD-produced diamond disks grown for microwave windows application, *Chem. Vap. Depos.* 20 (2014) 32–38.
- [28] A. Chayahara, Y. Mokuno, Y. Horino, Y. Takasu, H. Kato, H. Yoshikawa, N. Fujimori, The effect of nitrogen addition during high-rate homoepitaxial growth of diamond by microwave plasma CVD, *Diam. Relat. Mater.* 13 (2004) 1954–1958.
- [29] A. Tallaire, A.T. Collins, D. Charles, J. Achard, R. Sussmann, A. Gicquel, M. E. Newton, A.M. Edmonds, R.J. Cruddace, Characterisation of high-quality thick single-crystal diamond grown by CVD with a low nitrogen addition, *Diam. Relat. Mater.* 15 (2006) 1700–1707.
- [30] J. Achard, F. Silva, O. Brinza, A. Tallaire, A. Gicquel, Coupled effect of nitrogen addition and surface temperature on the morphology and the kinetics of thick CVD diamond single crystals, *Diam. Relat. Mater.* 16 (2007) 685–689.
- [31] H. Watanabe, T. Kitamura, S. Nakashima, S. Shikata, Cathodoluminescence characterization of a nitrogen-doped homoepitaxial diamond thin film, *J. Appl. Phys.* 105 (2009), 093529.
- [32] S. Dunst, H. Sternschulte, M. Schreck, Growth rate enhancement by nitrogen in diamond chemical vapor deposition – a catalytic effect, *Appl. Phys. Lett.* 94 (2009), 224101.
- [33] H. Yamada, A. Chayahara, Y. Mokuno, Effects of intentionally introduced nitrogen and substrate temperature on growth of diamond bulk single crystals, *Jpn. J. Appl. Phys.* 55 (2016), 01AC07 and references therein.
- [34] M.N.R. Ashfold, J.P. Goss, B.L. Green, P.W. May, M.E. Newton, C.V. Peaker, Nitrogen in diamond, *Chem. Rev.* 120 (2020) 5745–5794 (and references therein).
- [35] B.S. Truscott, M.W. Kelly, K.J. Potter, M. Johnson, M.N.R. Ashfold, Yu. A. Mankelevich, Microwave plasma enhanced chemical vapour deposition of nitrogen doped diamond, I: N₂/H₂ and NH₃/H₂ plasmas, *J. Phys. Chem. A* 119 (2015) 12962–12976.
- [36] L.M. Oberg, M. Batzer, A. Stacey, M.W. Doherty, Nitrogen overgrowth as a catalytic mechanism during diamond chemical vapour deposition, *Carbon* 178 (2021) 606–615 (and references therein).
- [37] J. Ma, J.C. Richley, M.N.R. Ashfold, Yu.A. Mankelevich, Probing the plasma chemistry in a microwave reactor used for diamond chemical vapour deposition by cavity ring down spectroscopy, *J. Appl. Phys.* 104 (2008), 103305.
- [38] J. Ma, M.N.R. Ashfold, Yu.A. Mankelevich, Validating optical emission spectroscopy as a diagnostic of microwave activated CH₄/Ar/H₂ plasmas used for diamond chemical vapor deposition, *J. Appl. Phys.* 105 (2009), 043302.
- [39] J.C. Richley, O.J.L. Fox, M.N.R. Ashfold, Yu.A. Mankelevich, Combined experimental and modeling studies of microwave activated CH₄/H₂/Ar plasmas for microcrystalline, nanocrystalline and ultrananocrystalline diamond deposition, *J. Appl. Phys.* 109 (2011), 063307.
- [40] E.J.D. Mahoney, B.S. Truscott, M.N.R. Ashfold, Yu.A. Mankelevich, Optical emission from C₂⁻ anions in microwave-activated CH₄/H₂ plasmas for chemical vapour deposition of diamond, *J. Phys. Chem. A* 121 (2017) 2760–2773.
- [41] E.J.D. Mahoney, B.S. Truscott, S. Mushtaq, M.N.R. Ashfold, Yu.A. Mankelevich, Spatially resolved optical emission and modeling studies of microwave-activated hydrogen plasmas operating under conditions relevant for diamond chemical vapour deposition, *J. Phys. Chem. A* 122 (2018) 8286–8300.
- [42] E.J.D. Mahoney, S. Mushtaq, M.N.R. Ashfold, Yu.A. Mankelevich, Combined spatially resolved optical emission and modeling studies of microwave-activated H₂/Ar and H₂/Kr plasmas operating at powers and pressures relevant for diamond chemical vapour deposition, *J. Phys. Chem. A* 123 (2019) 2544–2558.
- [43] J. Ma, Exploration of the Gas Phase Chemistry in Microwave Activated Plasmas Used for Diamond Chemical Vapour Deposition, Ph.D. Thesis., University of Bristol, 2008.
- [44] Yu.A. Mankelevich, P.W. May, New insights into the mechanism of CVD diamond growth: single crystal diamond in MW PECVD reactors, *Diam. Relat. Mater.* 17 (2008) 1021–1028.
- [45] A. Gicquel, N. Derkaoui, C. Rond, F. Benedic, G. Cicala, D. Moneger, K. Hassouni, Quantitative analysis of diamond deposition reactor efficiency, *Chem. Phys.* 398 (2012) 239–247.
- [46] M.S. Smoluchowski, On conduction of heat by rarefied gases, *Lond. Edinb. Dublin Philos. Mag. J. Sci.* 46 (1898) 192–206.
- [47] S. Song, M.M. Yovanovich, Correlation of thermal accommodation coefficient for ‘engineering’ surfaces, in: *Fundamentals of Conduction and Recent Developments in Contact Resistance ASME HTD* 69, 1987, pp. 107–116.
- [48] P.W. May, M.N.R. Ashfold, Yu.A. Mankelevich, Microcrystalline, nanocrystalline and ultrananocrystalline diamond chemical vapor deposition: experiment and modeling of the factors controlling growth rate, nucleation, and crystal size, *J. Appl. Phys.* 101 (2007), 053115.
- [49] S. Skokov, B. Weiner, M. Frenklach, Elementary reaction mechanism for growth of diamond (100) surfaces from methyl radicals, *J. Phys. Chem.* 98 (1994) 7073–7082.
- [50] G.P. Smith, D.M. Golden, M. Frenklach, N.W. Moriarty, B. Eiteneer, M. Goldenburg, C.T. Bowman, R.K. Hanson, S. Song, W.C. Gardiner Jr., et al., *GRI-Mech 3.0*, Available at, http://www.me.berkeley.edu/gri_mech/, accessed 2016.
- [51] M. Eckert, E. Neyts, A. Bogaerts, On the reaction behaviour of hydrocarbon species at diamond (100) and (111) surfaces: a molecular dynamics investigation, *J. Phys. D – Appl. Phys.* 41 (2008), 032006.
- [52] M. Frenklach, S. Skokov, Surface migration in diamond growth, *J. Phys. Chem. B* 101 (1997) 3025–3036.
- [53] A. Cheesman, J.N. Harvey, M.N.R. Ashfold, Studies of carbon incorporation on the diamond {100} surface during chemical vapor deposition using density functional theory, *J. Phys. Chem. A* 112 (2008) 11436–11448.
- [54] A. Netto, M. Frenklach, Kinetic Monte Carlo simulations of CVD diamond growth - interplay among growth, etching, and migration, *Diam. Relat. Mater.* 14 (2005) 1630–1646.
- [55] P.W. May, N.L. Allan, M.N.R. Ashfold, J.C. Richley, Yu.A. Mankelevich, Simplified Monte Carlo simulations of chemical vapour deposition diamond growth, *J. Phys. Condens. Matter* 21 (2009), 364203.
- [56] P.W. May, J.N. Harvey, N.L. Allan, J.C. Richley, Yu.A. Mankelevich, Simulations of chemical vapor deposition diamond film growth using a kinetic Monte Carlo model, *J. Appl. Phys.* 108 (2010), 014905.
- [57] W.J. Rodgers, P.W. May, N.L. Allan, J.N. Harvey, Three-dimensional kinetic Monte Carlo simulations of diamond chemical vapor deposition, *J. Chem. Phys.* 142 (2015), 214707.
- [58] A. Valentin, O. Brinza, S. Farhat, J. Achard, F. Benedic, 3D kinetic Monte-Carlo simulations of diamond growth on (100) surfaces, *Diam. Relat. Mater.* 123 (2022), 108865.
- [59] A. Croot, E.J.D. Mahoney, H. Dominguez-Andrade, M.N.R. Ashfold, N.A. Fox, Diamond chemical vapor deposition using a zero-total gas flow environment, *Diam. Relat. Mater.* 109 (2020), 108011.
- [60] P.W. May, Yu.A. Mankelevich, From ultrananocrystalline diamond to single crystal diamond growth in hot filament and microwave plasma-enhanced CVD reactors: a unified model for growth rates and grain sizes, *J. Phys. Chem. C* 112 (2008) 12432–12441.
- [61] Yu.A. Mankelevich, P.W. May, New insights into the mechanism of CVD diamond growth: Single crystal diamond in MW PECVD reactors, *Diam. Relat. Mater.* 17 (2008) 1021–1028.
- [62] T. Frauenheim, G. Jungnickel, P. Sitch, M. Kaukonen, F. Weich, J. Widany, D. Porezag, A molecular dynamics study of N-incorporation into carbon systems: doping, diamond growth and nitride formation, *Diam. Relat. Mater.* 7 (1998) 348–355.
- [63] M. Kaukonen, P.K. Sitch, G. Jungnickel, R.M. Nieminen, S. Poykko, D. Porezag, T. Frauenheim, Effect of N and B doping on the growth of CVD diamond (100): H (2×1) surfaces, *Phys. Rev. B* 57 (1998) 9965–9970.
- [64] J.E. Butler, I. Oleynik, A mechanism for crystal twinning in the growth of diamond by chemical vapour deposition, *Phil. Trans. R. Soc. A* 366 (2008) 295–310.
- [65] T. Van Regemorter, K. Larsson, A theoretical study of nitrogen-induced effects on initial steps of diamond CVD growth, *Chem. Vap. Depos.* 14 (2008) 224–231.
- [66] T. Van Regemorter, K. Larsson, Effect of substitutional N on important chemical vapor deposition diamond growth steps, *J. Phys. Chem. A* 113 (2009) 3274–3284.

- [67] T. Van Regemorter, K. Larsson, Effect of a NH coadsorbate on the CH₃ (or CH₂) adsorption to a surface step on diamond (100), *J. Phys. Chem. C* 113 (2009) 19891–19896.
- [68] Z. Yiming, F. Larsson, K. Larsson, Effect of CVD diamond growth by doping with nitrogen, *Theor. Chem. Accounts* 133 (2013) 1432.
- [69] B.J. Garrison, E.J. Dawnkaski, D. Srivistava, D.W. Brenner, Molecular dynamics simulations of dimer opening on a diamond {001}(2×1) surface, *Science* 255 (1992) 835–838.
- [70] F.K. de Theije, J.J. Schermer, W.J.P. van Enkevort, Effects of nitrogen impurities on the CVD growth of diamond: step bunching in theory and experiment, *Diam. Relat. Mater.* 9 (2000) 1439–1449.